Chapter 10

The Greening Earth

Piao et al.

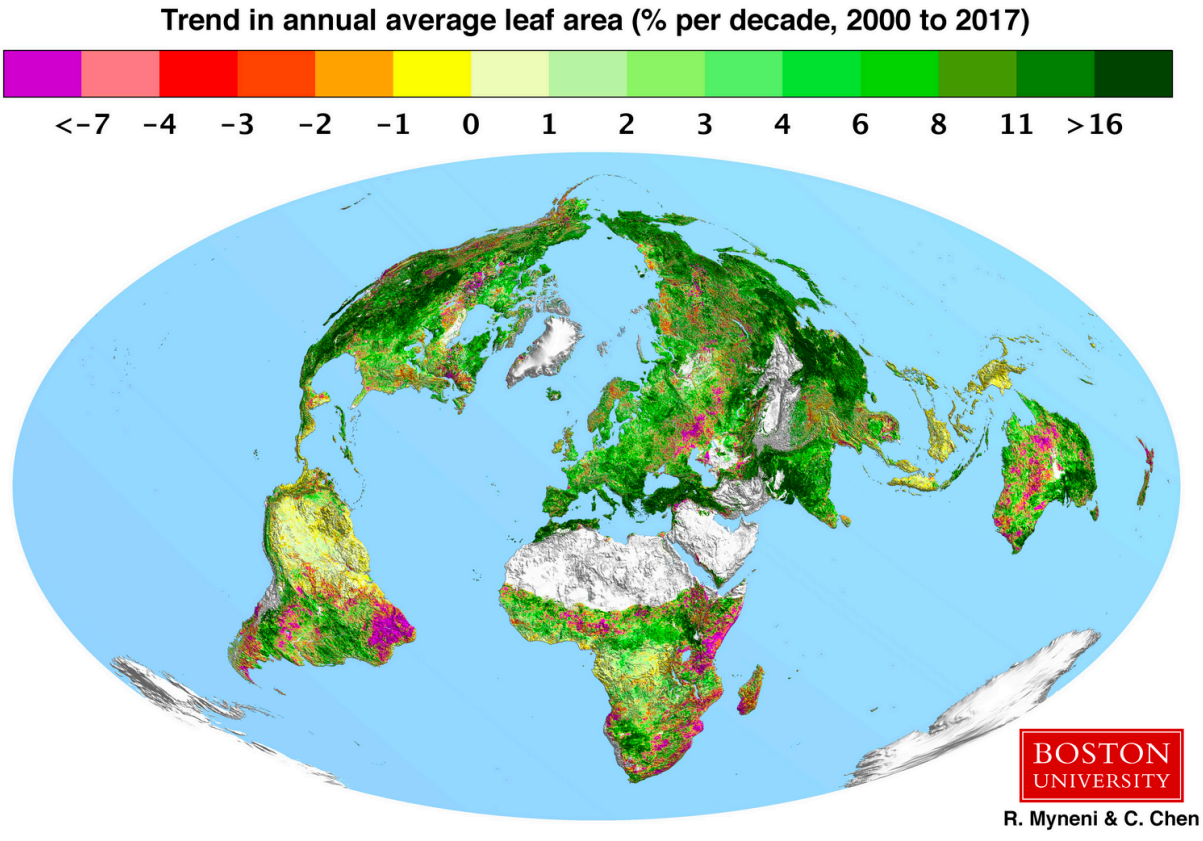

Characteristics, drivers and feedbacks of global greening

Shilong Piao[1,2,3], Xuhui Wang[1], Taejin Park[4], Chi Chen[4], Xu Lian[1], Yue He[1], Jarle W. Bjerke[5], Anping Chen[6], Philippe Ciais[1,7], Hans Tømmervik[5], Ramakrishna R. Nemani[8] and Ranga B. Myneni[4]*

Q1 Abstract | Vegetation greenness has been increasing globally since at least 1981, when satellite technology enabled large-scale vegetation monitoring. The greening phenomenon, together with warming, sea-level rise and sea-ice decline, represents highly credible evidence of anthropogenic climate change. In this Review, we examine the detection of the greening signal, its causes and its consequences. Simulations with vegetation models revealed that CO_2 fertilization was the main driver of greening on the global scale, with climate change, increased nitrogen deposition and land-use change also notable drivers at the regional scale. Modelling indicated that greening could mitigate global warming by increasing the carbon sink on land and altering biogeophysical processes, mainly evaporative cooling. Coupling high temporal and fine spatial resolution remote observations with ground measurements, increasing sampling in the tropics and Arctic, and modelling Earth systems in more detail will further our insights into the greening of Earth.

Afforestation
The conversion of treeless lands to forests through planting trees.

Greening
An increasing trend in vegetation greenness.

Vegetation controls the exchange of carbon, water, momentum and energy between the land and the atmosphere, and provides food, fibre, fuel and other valuable ecosystem services[1,2]. Changes in vegetation structure and function are driven by climatic and environmental changes, and by human activities such as land-use change. Given that increased carbon storage in vegetation, such as through afforestation, could combat climate change[3,4], quantifying vegetation change and its impact on carbon storage and climate has elicited considerable interest from scientists and policymakers.

However, it is not possible to detect vegetation changes at the global scale using ground-based observations due to the heterogeneity of change and the lack of observations that can detect these changes both spatially and temporally. While monitoring the changes in some vegetation properties (for example, stem-size distribution and below-ground biomass) at the global scale remains impossible, satellite-based remote sensing has enabled continuous estimation of a few important metrics, including vegetation greenness, since the 1980s (BOX 1).

In 1986, a pioneering study by Tucker et al.[5] on remotely sensed normalized difference vegetation index (NDVI; a radiometric measure of vegetation greenness) (BOX 1) revealed a close connection between vegetation canopy greenness and photosynthesis activity (as inferred from seasonal variations in atmospheric CO_2 concentration). This index was successfully used to constrain vegetation primary production globally[6]. Using NDVI data from 1981 to 1991, Myneni et al.[7] reported an increasing trend in vegetation greenness in the Northern Hemisphere, which was subsequently observed across the globe[8–13]. This 'vegetation greening' is defined as a statistically significant increase in annual or seasonal vegetation greenness at a location resulting, for instance, from increases in average leaf size, leaf number per plant, plant density, species composition, duration of green-leaf presence due to changes in the growing season and increases in the number of crops grown per year.

There has also been considerable interest in understanding the mechanisms or drivers of greening[11,14]. Lucht et al.[14] and Xu et al.[10] revealed that warming has eased climatic constraints, facilitating increasing vegetation greenness over the high latitudes. Zhu et al.[11] further investigated key drivers of greenness trends and concluded that CO_2 fertilization is a major factor driving vegetation greening at the global scale. Subsequent studies based on fine-resolution and medium-resolution satellite data[13] have shown the critical role of land-surface history, including afforestation and agricultural intensification, in enhancing vegetation greenness. The large spatial scale of vegetation greening and the robustness of its signal have led the Intergovernmental Panel on Climate Change (IPCC) special report on climate change and land[15] to list it, together with global-scale warming, sea-level rise[16] and sea-ice decline[16], as highly credible evidence of the environmental impact of anthropogenic climate change.

Greener vegetation not only results from climate and atmospheric changes but also feeds back to the climate

*e-mail: slpiao@pku.edu.cn

https://doi.org/10.1038/s43017-019-0001-x

Key points

- Long-term satellite records reveal a significant global greening of vegetated areas since the 1980s, which recent data suggest has continued past 2010.
- Pronounced greening is observed in China and India due to afforestation and agricultural intensification.
- Simplified global vegetation models suggest that CO_2 fertilization is the main driver of global vegetation greening.
- Warming is the major cause of greening in boreal and Arctic biomes, but has negative effects on greening in the tropics.
- Greening was found to mitigate global warming through enhanced land carbon uptake and evaporative cooling, but could also lead to decreased albedo that could potentially cause local warming.
- Greening enhances transpiration, a process that reduces soil moisture and runoff locally, but can either amplify or reduce runoff and soil moisture regionally.

Browning
A decreasing trend in vegetation greenness.

through biogeochemical and biogeophysical processes. These feedbacks are often studied with Earth system models (ESMs), in which vegetation is coupled with the atmosphere and the hydrologic cycle[17]. ESM-based studies have demonstrated that greening can accelerate the hydrologic cycle by increasing the amount of water transpired by plants, alter the energy exchange between land and the atmosphere, and affect atmospheric circulation patterns[18,19].

In this Review, we synthesize past and recent efforts to characterize the spatiotemporal patterns of vegetation greening since the 1980s. We discuss how rising atmospheric CO_2 concentration, climate change, land-use change and nitrogen deposition are the key drivers of greenness changes on the global and regional scale. We assess the impacts of vegetation greening on carbon, water and energy balances, and conclude by identifying key challenges and perspectives for future research.

Greenness changes

Global-scale vegetation greening has been demonstrated using nearly four decades of NDVI and leaf area index (LAI) greenness data derived from the Advanced Very-High-Resolution Radiometer (AVHRR) instrument (FIG. 1a,b). While early studies primarily used the NDVI to detect changes in global greenness, recent studies widely use the LAI, since it has clear physical interpretation and is a fundamental variable in almost all land-surface models (BOX 1). An ensemble of LAI datasets has shown that 52% ($P<0.05$) to 59% ($P<0.10$) of global vegetated lands displayed an increasing trend in growing season LAI since the 1980s[11] (FIG. 1a). Although some studies reported a stalling, or even a reversal, of the greening trend since 2000 based on AVHRR[20] and collection 5 (C5) of the Moderate Resolution Imaging Spectroradiometer (MODIS) data[21], this signal might be an artefact of sensor degradation and/or processing[22–24]. For example, using a revised calibration of the MODIS data in the most recent collection 6 (C6) dataset[24], Chen et al.[13] showed that leaf area increased by 5.4 million km^2 over 2000–2017, an area equivalent to the areal extent of the Amazon rainforest[13]. Indeed, 34% of vegetation land exhibited greening ($P<0.10$), whereas only 5% experienced browning ($P<0.10$).

New satellite-based vegetation indices also support the global greening trend observed since 2000 (FIG. 1), including the enhanced vegetation index (EVI) and near-infrared reflectance of terrestrial vegetation (NIRv) (BOX 1). However, while vegetation greenness is increasing at the global scale, the changes vary considerably between regions and seasons.

Regional trends. In the high northern latitudes (>50°N), AVHRR and Landsat records indicate a widespread increase in vegetation greenness since the 1980s[8,12,25] (FIG. 2a–d). Regions with the greatest greening trend include northern Alaska and Canada, the low-Arctic parts of eastern Canada and Siberia, and regions of Scandinavia[12,25,26]. Dendrochronological data and photographic evidence further corroborate these findings[27–30]. In general, the LAI over high northern latitudes will continue to increase by the end of this century[31], based on the results of an ensemble of ESMs (FIG. 2e–h). While only a 3% area of the high latitudes shows browning during 1982–2014 (REF.[25]), there is a growing proportion of Arctic areas exhibiting a browning trend[32]. Such trends first emerged in boreal forests, where a multitude of disturbances (for example, fires, harvesting and insect defoliation) prevail[9,33–37]. The North American boreal forests in particular exhibit browning areas nearly 20 times larger than the Eurasian boreal forests, showing heterogeneous regional greenness change[38].

The northern temperate region (25–50°N) is another vegetation greening hotspot, experiencing faster rates of greening than the high latitudes since 2000 (FIG. 2b,d). Indeed, ~14 million km^2 of the temperate region greened ($P<0.10$), contributing about one-half of the global net leaf area increase over this time period[13]. The increase of vegetation greenness is especially strong in agricultural regions (for example, India[13]) and recently afforested areas (for example, China[13,39]); collectively, China and India alone contribute more than 30% of the total net increase in the global LAI[13].

Tropical regions (25°S–25°N) are also greening (FIG. 2b,d), contributing about a quarter of the net global increase in leaf area since 2000 (REF.[13]). However, the tropics also have areas where significant browning was reported, for example, in the Brazilian Cerrado and Caatinga regions and Congolian forests[13,40]. It is worth noting that substantial uncertainties remain in the tropical vegetation greenness estimations due to the saturation effects of greenness indices in dense vegetation[41] and contamination by clouds and aerosols[42]. These

Author addresses

[1]Sino-French Institute for Earth System Science, College of Urban and Environmental Sciences, Peking University, Beijing, China.
[2]Key Laboratory of Alpine Ecology, Institute of Tibetan Plateau Research, Chinese Academy of Sciences, Beijing, China.
[3]Center for Excellence in Tibetan Earth Science, Chinese Academy of Sciences, Beijing, China.
[4]Department of Earth and Environment, Boston University, Boston, MA, USA.
[5]Norwegian Institute for Nature Research, FRAM – High North Research Centre for Climate and the Environment, Tromsø, Norway.
[6]Department of Biology, Colorado State University, Fort Collins, CO, USA.
[7]Laboratoire des Sciences du Climat et de l'Environnement, CEA CNRS UVSQ, Gif-sur-Yvette, France.
[8]NASA Ames Research Center, Moffett Field, CA, USA.

Box 1 | **Remotely sensed vegetation greenness**

Remotely sensed vegetation greenness generally refers to spectral vegetation indices (VIs) or the leaf area index (LAI). Photosynthetic pigments in plant leaves (mainly chlorophyll and carotenoids) strongly absorb photosynthetically active radiation, which largely overlaps with the visible spectrum (400–700 nm), particularly red wavelengths (620–700 nm). In the near-infrared (NIR) domain (700–1,300 nm), absorbance by leaf constituents is either small or absent; thus, scattering increases the likelihood that photons will exit the leaf. This is the biophysical basis for high leaf-level reflectance in the NIR region. At the canopy scale, structural properties such as LAI and leaf-angle distribution dominate variability in NIR reflectance[176]. This unique spectral signature of vegetation in the red and NIR channels, a characteristic not present in common, non-vegetative features such as soil, snow and water[177,178], has thus been utilized to derive numerical VIs measuring vegetation greenness[176,179,180] (Supplementary Table S1). For example, the normalized difference vegetation index, which is one of the most widely used VIs in assessing vegetation greenness and its changes from local to global scales (Supplementary Table S2), is useful for measuring canopy structural properties, such as leaf area, light interception and biomass[41,181,182]. Satellite sensors, such as the Advanced Very-High-Resolution Radiometer (AVHRR), Moderate Resolution Imaging Spectroradiometer (MODIS), Vegetation, Medium Resolution Imaging Spectrometer (MERIS) and Visible Infrared Imaging Radiometer Suite (VIIRS), have been deployed with varying temporal coverage, providing VI products based on a wide range of spectral-band specifications and data processing (Supplementary Table S3). For example, the AVHRR does not have a blue channel, so this sensor is unable to produce blue-band-based greenness indices like the enhanced vegetation index. These sensor differences make it a non-trivial challenge to produce consistent and continuing long-term greenness products[183].

Compared with VIs, the LAI (the one-sided green leaf area per unit ground area in broadleaf canopies or one-half of the total needle surface area per unit ground area in coniferous canopies[184,185]) is a well-defined physical attribute of vegetation. The LAI is a state variable in all land models and key to quantifying the exchanges of mass, momentum and energy between the surface and the atmosphere. Multiple approaches for retrieving the LAI from remote sensing data have been developed — these can be conceptually categorized as: empirical approaches that are based on relationships between VIs and the LAI[186,187]; machine-learning approaches that train surface reflectance or VIs to given reference LAIs[182,188,189]; and physical approaches that are based on the physics of radiation interaction with elements of a canopy and transport within the vegetative medium[7,184,190,191]. See Supplementary Table S4 for currently available global LAI products.

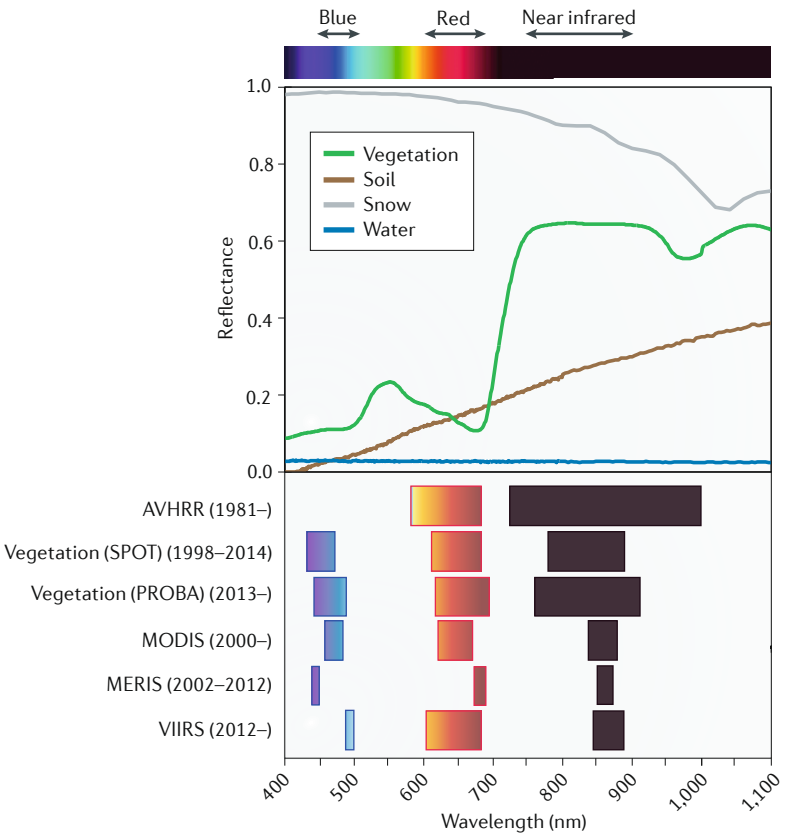

uncertainties partly underlay the disagreement between the MODIS and AVHRR products[13] when measuring tropical greenness and the debate on whether the Amazonian forests have greened or browned in response to droughts[42–44].

The extratropical Southern Hemisphere (>25°S) experienced a general greening trend since the 1980s[13,45], but this is lower than experienced in the temperate and high-latitude Northern Hemisphere[13] (FIG. 2a–d). Regional greening hotspots in southern Brazil and southeast Australia mostly overlap with the intensive cropping areas[13], highlighting the increasing contribution of managed ecosystems to vegetation greening. Note that most of this region is dominated by semi-arid ecosystems[46], where vegetation coverage is generally sparse. Thus, satellite vegetation indices over this region are generally sensitive to change in soil background. For example, browning was detected from the AVHRR dataset since the 2000s[20] (FIG. 2b), but MODIS C6 data (which is better calibrated and can distinguish vegetation from background more accurately) instead showed an overall greening trend particularly since 2002 (REF.[13]; FIG. 2c,d).

Seasonal changes of greenness. In the northern temperate and high latitudes, greenness often shows distinctive seasonal patterns within a calendar year (FIG. 3). Several metrics of land-surface phenology have been developed to depict the seasonal cycle of greenness[47], including the widely used start of the growing season (SOS) and end of the growing season (EOS)[48]. Although phenology dates can vary depending on the greenness product or algorithm used[49–51], significant trends towards both earlier SOS (2–8 days decade^{-1}) and later EOS (1–6 days decade^{-1}) and, thus, longer lengths of the growing season (LOS) (2–10 days decade^{-1}), have been observed in most Northern Hemisphere regions during the past four decades[7,8,25,52–54] (FIG. 3a–c). These trends are corroborated by ground-based observation data in spring and autumn[55–57]. The increase in LOS is driven mainly by an advanced SOS in Eurasia (53–81% of LOS lengthening is due to SOS advance) and delayed EOS in North America (57–96% of LOS lengthening is due to EOS delay), with the more rapid total LOS increase seen in Eurasia[25,58–60].

In addition to longer growing seasons, satellite greenness data also reveal important shifts in the timing and magnitude of the seasonal peak greenness[47,61]. For example, the timing of peak greenness has advanced by 1.2 days decade^{-1} during 1982–2015 (REF.[62]) and 1.7 days decade^{-1} during 2000–2016 (REF.[61]) over the extratropical Northern Hemisphere (FIG. 3a), with the boreal region peak greenness advancing twice as fast as the Arctic tundra and temperate ecosystem peaks[61]. Since the 1980s, the magnitude of the peak greenness has also increased over the extratropical Northern Hemisphere by ~0.1 standardized NDVI anomaly per year[62], with a stronger signal in the pan-Arctic region[63,64].

Phenology changes, including the SOS advancement, EOS delay and peak greenness enhancement, can significantly change the Earth's seasonal landscape. Northern high latitudes, which traditionally have high seasonality

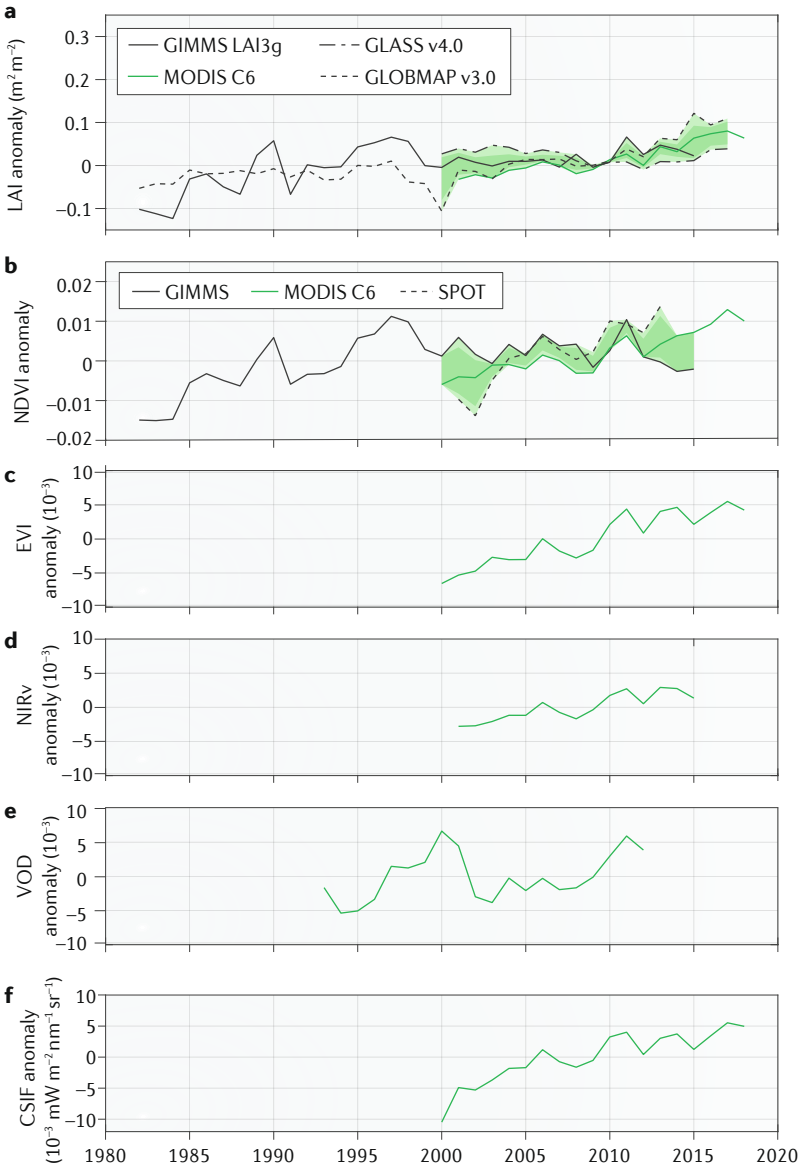

Fig. 1 | **Changes in satellite-derived global vegetation indices, vegetation optical depth and contiguous solar-induced fluorescence. a** | Leaf area index (LAI) from four products: GIMMS[13], GLASS[192], GLOBMAP[23] and Moderate Resolution Imaging Spectroradiometer (MODIS) C6 (REF.[193]). **b** | Normalized difference vegetation index (NDVI) from three products: GIMMS[194], MODIS C6 (REF.[195]) and SPOT[196]. **c** | Enhanced vegetation index (EVI) from MODIS C6 (REF.[195]). **d** | Near-infrared reflectance of terrestrial vegetation (NIRv)[197]. **e** | Vegetation optical depth (VOD)[119]. **f** | Contiguous solar-induced fluorescence (CSIF)[114]. In parts **a** and **b**, the light-green shading denotes the range of LAI and NDVI across different products and the dark-green shading denotes the interquartile range (between the 25th and 75th percentiles). Only measurements during the growing season[11] were considered.

Land-surface phenology
Cyclic phenomena in vegetated land surfaces observed from remote sensing.

Carboxylation
The addition of CO_2 to ribulose-1,5-bisphosphate during photosynthesis.

(that is, short and intense growing seasons), are exhibiting seasonality similar to that of their counterparts 6° to 7° south in the 1980s. In other words, the latitudinal isolines of northern vegetation seasonality have shifted southward since the 1980s. The diminished seasonality of the northern high-latitude vegetation[10] is consistent with changes in the velocity of vegetation greenness (defined as the ratio of temporal greenness change to its spatial gradient)[65], which showed faster northward movement of the SOS (3.6 ± 1.0 km year^{-1}) and the EOS (6.0 ± 1.1 km year^{-1}) than the peak greenness (3.1 ± 1.0 km year^{-1}) during 1982–2011 (REF.[65]).

Fig. 2 | **Spatial patterns of changes in leaf area index.** **a** | Growing season (GS) mean Advanced Very-High-Resolution Radiometer (AVHRR) leaf area index (LAI) trend during 1982–2009. The AVHRR LAI dataset is the average of three different products (GIMMS[13], GLOBMAP[23] and GLASS[192]). **b** | Change in the GS mean AVHRR LAI over four regions during 1982–2009. **c** | GS mean Moderate Resolution Imaging Spectroradiometer (MODIS) LAI during 2000–2018. **d** | Change in the GS mean MODIS LAI over four regions during 2000–2018. MODIS LAI is from collection 6 (REF.[193]). **e** | Relative change in GS mean LAI between 1981–2000 and 2081–2100 under the Representative Concentration Pathway 2.6 (RCP2.6), based on the Coupled Model Intercomparison Project Phase 5 (CMIP5) multi-model ensemble. **f** | Relative change in GS mean CMIP5 LAI between 2018–2100 under RCP2.6, relative to 1981–2000. **g** | Relative change in GS mean LAI between 1981–2000 and 2081–2100 under RCP8.5, based on CMIP5. **h** | Relative change in GS mean CMIP5 LAI between 2018–2100 under RCP8.5, relative to 1981–2000. The number of CMIP5 models used in the calculation of the multi-model mean is 16 and 19, for RCP2.6 and RCP8.5, respectively (Supplementary Table S5). In parts **a**, **c**, **e** and **g**, the white land areas depict barren lands, permanent ice-covered areas, permanent wetlands, built-up areas and water. In parts **b**, **d**, **f** and **h**, blue represents the high-latitude Northern Hemisphere (NH) (50–90°N), green represents the temperate NH (25–50°N), purple represents the tropical zone (25°S–25°N) and yellow represents the extratropical Southern Hemisphere (SH) (90–25°S). The shading shows the ±1 inter-model standard deviation.

Drivers of greening

Several factors are thought to impact vegetation greening, including rising atmospheric CO_2 concentrations, climate change, nitrogen deposition and land-use changes. However, nonlinear impacts and interactions make it challenging to quantify the individual contribution of these factors to the observed greening trend. In this section, we review the contribution of several key drivers of vegetation greening and efforts to quantitatively attribute the observed greening trend to each of these factors.

CO_2 fertilization. As CO_2 is the substrate for photosynthesis, rising atmospheric CO_2 concentration can enhance photosynthesis[66] by accelerating the rate of carboxylation; this process is known as the 'CO_2 fertilization effect'. In addition, increased CO_2 concentrations can also enhance vegetation greenness by partially closing leaf stomata, leading to enhanced water-use efficiency[67], which should relax water limitation to plant growth, particularly over semi-arid regions[45,68,69]. Analysis of the 'Trends and drivers of the regional-scale sources and sinks of carbon dioxide' (TRENDY) ensemble of dynamic global vegetation models (DGVMs)[70] suggests that rising CO_2 is the dominant driver of vegetation greening, accounting for nearly 70% of global LAI trend since the 1980s[11] (FIG. 4). Statistical modelling also supports the important role of rising atmospheric CO_2 concentration in driving vegetation greening[71,72]. Free-air CO_2 enrichment (FACE) experiments show that

1982–2009 (GIMMS, GLOBMAP and GLASS mean)

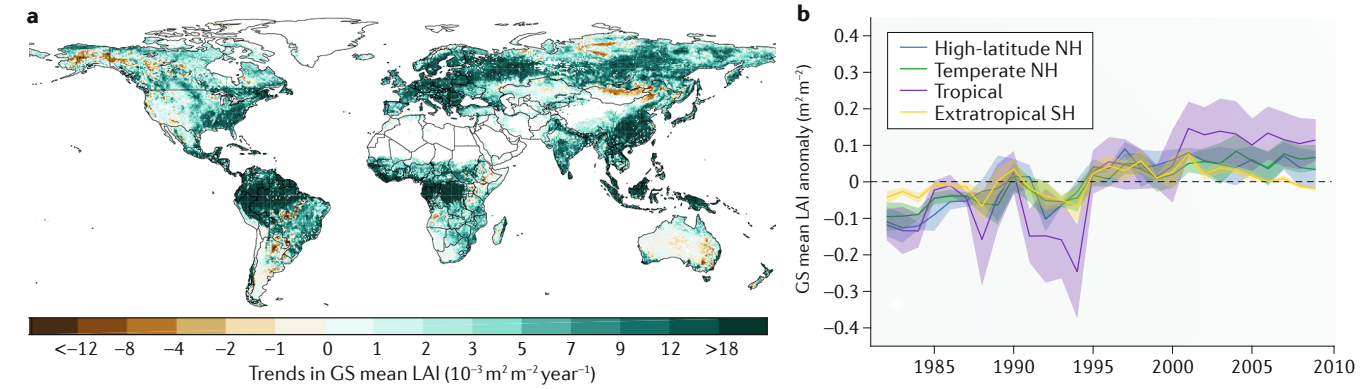

2000–2018 (MODIS)

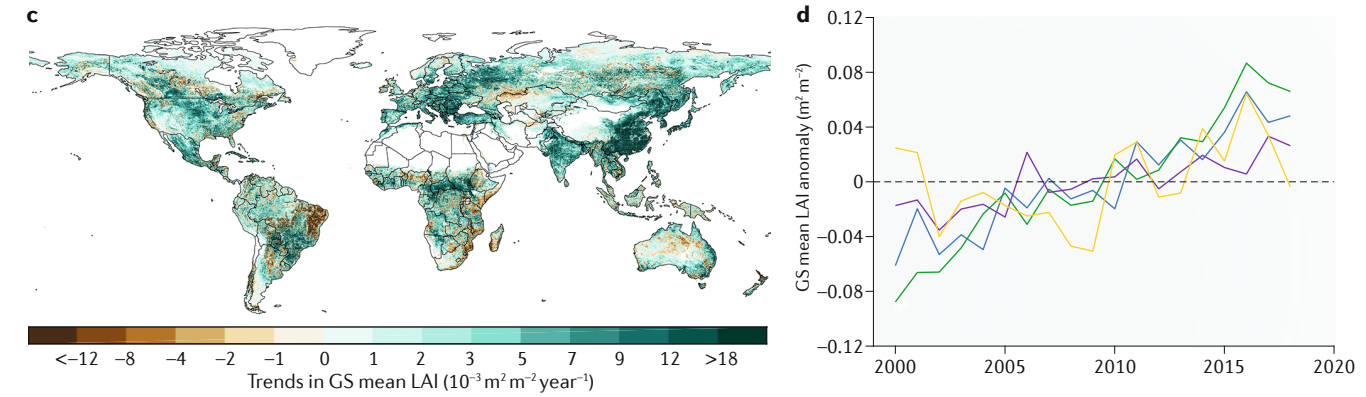

2081–2100 relative to 1981–2000, RCP2.6

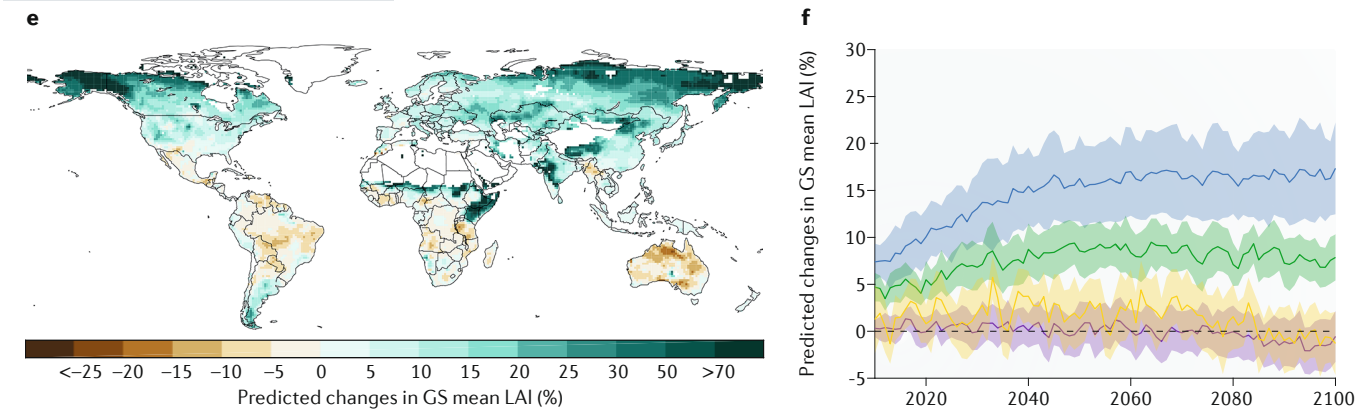

2081–2100 relative to 1981–2000, RCP8.5

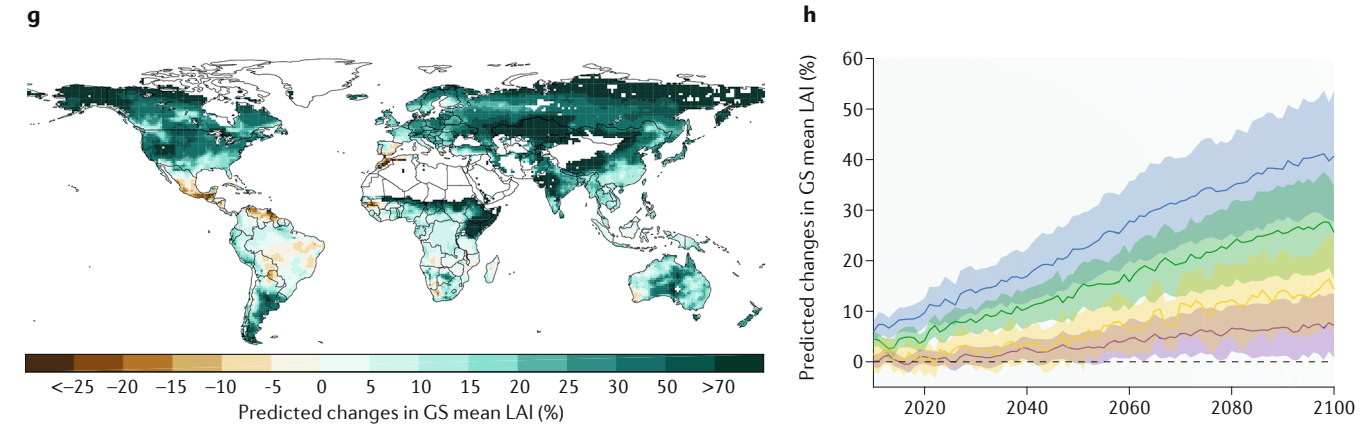

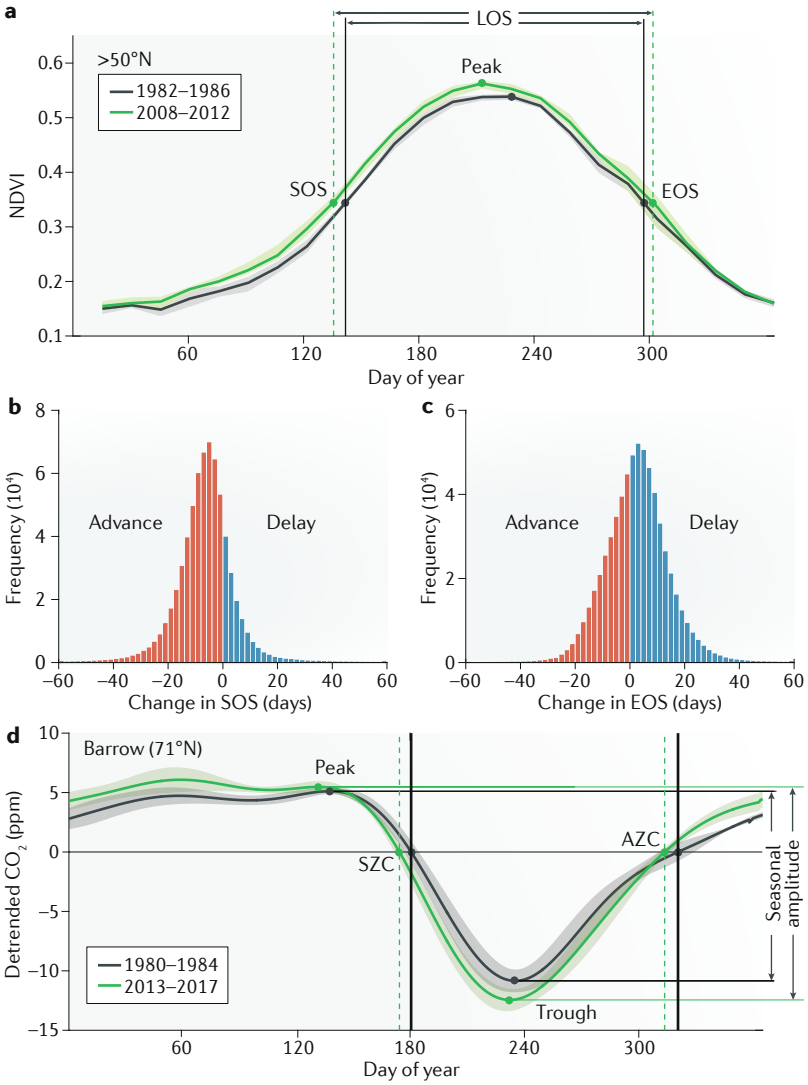

Fig. 3 | **Changes in the seasonality of vegetation greenness and atmospheric CO_2 concentration. a** | Five-year mean seasonal variations of the normalized difference vegetation index (NDVI) over Northern Hemisphere high latitudes (>50°N) during 1982–1986 (black line) and 2008–2012 (green line). Start of the growing season (SOS) and end of the growing season (EOS) are shown as 50% of the maximum NDVI. The length of the growing season (LOS) is the difference between the EOS and the SOS. **b** | Frequency distribution of SOS change in the Northern Hemisphere during 1982–2012. **c** | Frequency distribution of EOS change in the Northern Hemisphere during 1982–2012. **d** | Five-year mean detrended seasonal CO_2 variations at Barrow, AK, USA (71°N) (NOAA ESRL archive: https://www.esrl.noaa.gov/gmd/ccgg/obspack/) during 1980–1984 (black line) and 2013–2017 (green line). Vertical lines mark the spring zero-crossing date (SZC) and autumn zero-crossing date (AZC). Horizontal lines mark the seasonal amplitude as the difference between the maximum and the minimum of detrended seasonal CO_2 variations. Shaded areas show the range of interannual variations in the NDVI in part **a** and the standard deviation of the detrended CO_2 mole fraction (ppm) in part **d** at the day of year. NDVI data are the updated dataset from Tucker et al.[194]. Parts **b** and **c** are adapted with permission from REF.[48], Wiley-VCH.

elevating the CO_2 concentration by ~200 ppm above the ambient conditions significantly enhances vegetation productivity[73] and increases leaf area[74]. Different plant species vary largely in the magnitude of LAI enhancement[75], with the larger effect on forest stands having lower LAI at the ambient conditions[76]. In DGVMs, elevated CO_2 increases vegetation productivity more in tropical ecosystems than in temperate and boreal ecosystems[11,77,78] (FIG. 4b). However, the strength of the CO_2 fertilization effect can be limited by extreme weather events[79,80] and nutrient and water availability[73,81,82]. Indeed, nitrogen and phosphorus have been shown to regulate the global pattern of CO_2 fertilization effects[83]. Since nutrient processes were under-represented in the ESMs used in the IPCC Fifth Assessment Report (AR5), the predictions of continued greening trends through 2100 (REF.[31]) (FIGS 2e–h,5) might overestimate the CO_2 fertilization effects.

Climate change. Although rising atmospheric CO_2 concentration is the main driver of global greening, climate change, such as anthropogenic warming and regional trends in precipitation, is a dominant driver of greenness changes over 28% of the global vegetated area[11]. The global contribution of climate change to increasing greenness is only 8% (FIG. 4a), however, because impacts of climate change on vegetation greenness vary between regions[11]. For example, warming could reduce vegetation growth in the tropics[84], where ambient temperature is close to vegetation optimal temperature[85], but warming significantly increases vegetation greenness in the boreal and Arctic regions[86] by enhancing metabolism[87] and extending the growing season[59,88,89]. DGVM simulations show that the positive effects of climate change, primarily from warmer temperature[14], dominate the greening trend over more than 55% of the northern high latitudes (FIG. 4b) and in the Tibetan Plateau[11]. However, this positive impact of anthropogenic warming on greenness appears to have weakened during the past four decades[90,91], when the correlation coefficient between temperature and greenness decreased by more than 50%[90,91], suggesting a possible saturation of future greening in response to warmer temperature.

In water-limited ecosystems, changes in precipitation — reflecting either decadal climate variability or trends from anthropogenic climate change — were suggested as the main driving factor of greening and browning[45,92]. Precipitation-driven greening is most evident in the African Sahel[93,94] and semi-arid ecosystems of southern Africa and Australia[45,95] (FIG. 4c). Both empirical models and DGVMs indicate that 'the greening Sahel', one of the early examples of vegetation greening detected by satellite measurements[93,94], was primarily driven by increases in precipitation after a severe drought in the early 1980s[96–98]. This causal relationship between precipitation and greenness changes was further supported through analyses of recent microwave satellite measurements and long-term field surveys[99,100].

Land-use change. Like climate change, land-use change exerts a considerable but highly spatially variable influence on greenness changes[11,13] (FIG. 4). Specifically, deforestation dominates the tropics[101,102], while afforestation increases forest area over temperate regions, particularly in China, where the forest area has increased by more than 20% since the 1980s[103]. The TRENDY ensemble of DGVMs[70] indicates that greenness changes over 19% of the northern temperate vegetation (25–50°N) are primarily driven by land-use change[11] (FIG. 4c). However, this might be an underestimate since critical land-use

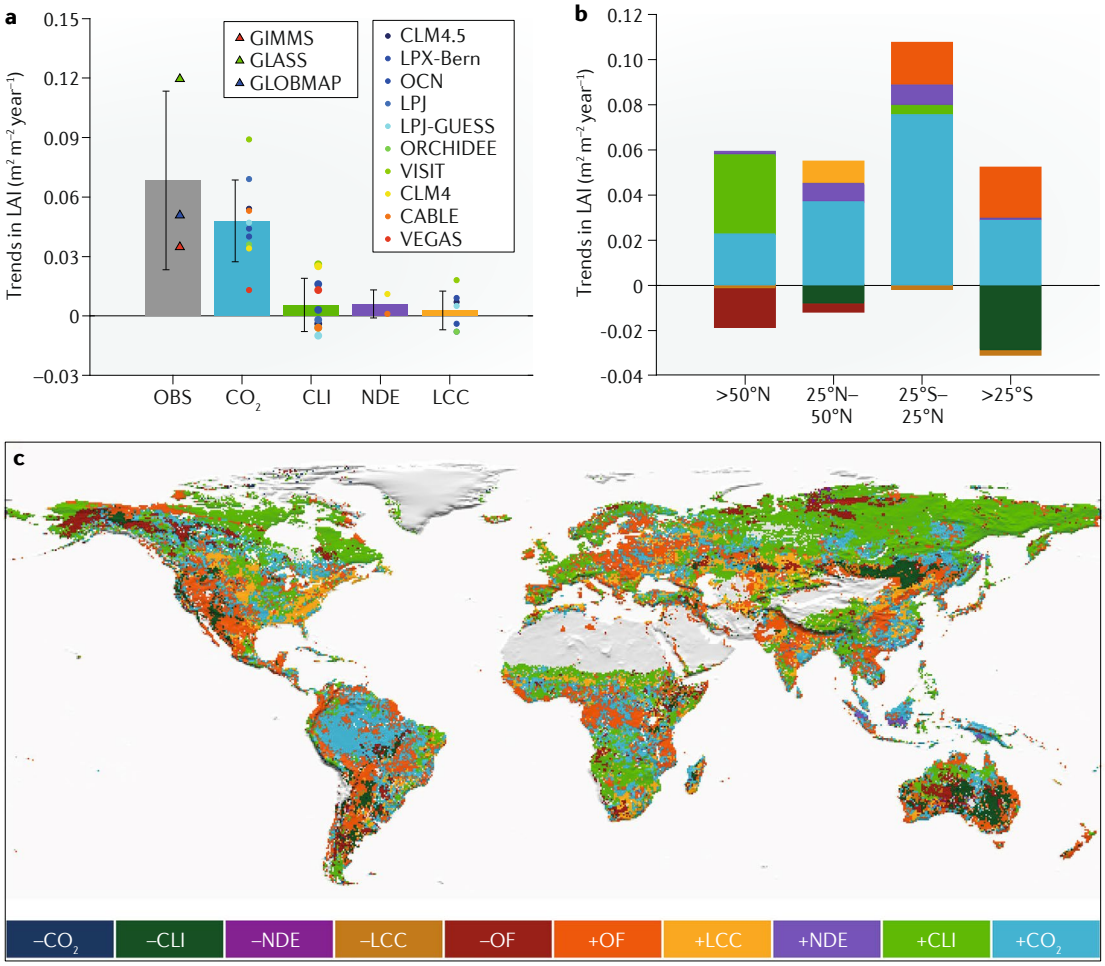

Fig. 4 | **Attribution of trends in growing season mean leaf area index. a** | Trends in the global-averaged leaf area index (LAI) derived from satellite observation (OBS) and attributed respectively to rising CO_2 (CO_2), climate change (CLI), nitrogen deposition (NDE) and land cover change (LCC) during 1982–2009 (REF.[11]). The error bars show the standard deviation of trends derived from satellite data and model simulations. Individual model-estimated contributions of each driver to LAI trends are shown as coloured dots. **b** | Contribution of different drivers to LAI change in latitude bands (>50°N, 25–50°N, 25°S–25°N, >25°S). **c** | Spatial distribution of the dominant driver of growing season mean LAI trend, defined as the driver that contributes the most to the increase (or decrease) in LAI in each vegetated grid cell. Other factors (OF) is defined by the fraction of the observed LAI trends not accounted for by modelled factors. Parts **b** and **c** share the same colour legend, where the '+' prefix indicates a positive effect from the corresponding driver on LAI trends and the '–' prefix indicates a negative effect. Data courtesy of Zhu et al.[11].Part **c** adapted from REF.[11], Springer Nature Limited.

processes[104,105] are under-represented or missing in the current generation of DGVMs. For example, forest-age dynamics are not represented in most DGVMs, even though one-third of the global forests are younger than 20 years old[106], implying that forest regrowth might contribute to global greening in the future. In addition, agricultural intensification with multiple cropping, irrigation and fertilizer usage must contribute considerably to vegetation greening, which is exemplified by the dominance of other unmodelled factors over agricultural lands of India, China and Eastern Europe (FIG. 4c).

Nitrogen deposition. Anthropogenic changes in the amount, rate and distribution of nitrogen deposition can impact greening patterns, since insufficient nitrogen availability can stunt plant growth[107–109], potentially slowing greening or causing browning, but excess nitrogen can enhance plant growth in nitrogen-limited systems[109]. However, the few DGVMs that include the nitrogen cycle do not indicate that nitrogen deposition plays a dominant driving role on the greening at either the global or regional scales (FIG. 4). Modelling studies differ on the contribution of increasing nitrogen deposition to the global LAI increase[11] (9 ± 12%), largely due to the incomplete representation of nitrogen-related processes[110]. A growing number of DGVMs are currently incorporating nitrogen processes[111], though, and future research priorities include better measurement and representation of processes such as plant nitrogen uptake and allocation[110].

Impact of greening on the carbon cycle

Greening increases the amount of photosynthetically active sunlight that is absorbed by vegetation and, thus, enhances productivity[112,113]. There has been substantial evidence showing enhanced vegetation productivity from contiguous solar-induced fluorescence (CSIF;

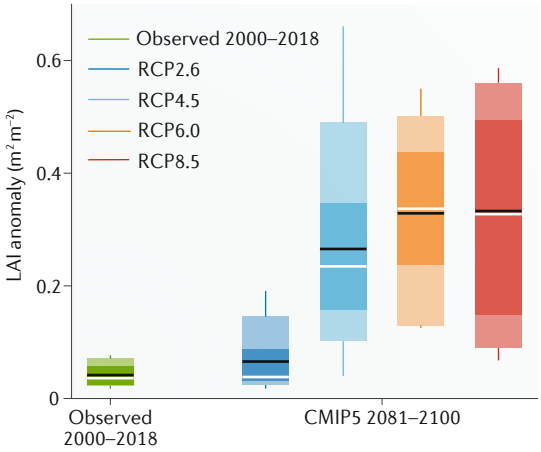

Fig. 5 | **Current and predicted global leaf area index.** Current leaf area index (LAI) anomaly ($m^2\ m^{-2}$) from an average of satellite measurements based on GIMMS[13], GLASS[192], GLOBMAP[23] and Moderate Resolution Imaging Spectroradiometer (MODIS) C6 (REF.[193]). Predicted LAI anomalies from the Coupled Model Intercomparison Project Phase 5 (CMIP5) multi-model (Supplementary Table S5) projections during 2081–2100. The boxes and whiskers indicate the minimum, 10th, 25th, 50th, 75th and 90th percentiles and the maximum LAI of CMIP5 models; the black and white lines indicate the mean and median LAI of CMIP5 models, respectively. LAI anomalies were calculated against the average during 1980–2005. RCP, Representative Concentration Pathway.

FIG. 1f) observations[114], empirical models of vegetation productivity[92,115] and DGVM and ESM simulations[70,116] (FIG. 6). It should be noted, though, that CSIF is not fully independent from MODIS greenness indices, since its derivation relies on both solar-induced fluorescence measurements from Orbiting Carbon Observatory 2 and MODIS reflectance measurements[114].

Enhanced vegetation productivity increases terrestrial carbon storage, slowing down anthropogenic climate warming[117]. For example, about 29% of the anthropogenic CO_2 emissions since the 1980s is offset by the land carbon sink (2.5 ± 1.0 PgC year^{-1})[111]. This vegetation-induced large land carbon sink was also inferred from forest inventories[118] and above-ground biomass estimated from the vegetation optical depth (FIG. 1e), a microwave-based satellite measurement of both woody and leaf biomass[119]. Multiple lines of evidence, including analyses from DGVMs, atmospheric inversion models and the residual land sink (the mass balance residual of anthropogenic CO_2 emissions, atmospheric CO_2 growth rate and ocean CO_2 budget), confirm the increasing magnitude of the global land carbon sink since the 1980s[111] (FIG. 6). An ecosystem model driven by satellite LAI measurements estimated that increased LAI accounts for 36% (0.4 PgC year^{-1}) of the land carbon sink enhancement of 1981–2016 (REF.[112]). Recent studies indicate that the trend in the land carbon sink has further accelerated since the late 1990s[120,121]. For example, the rate of update during 1998–2012 was three times that of 1980–1988 (0.17 PgC year^{-2} in comparison with 0.05 PgC year^{-2})[121], attributed to afforestation-induced greening in the temperate Northern Hemisphere[13,121]. These hotspots of afforestation and forest regrowth are in accordance with the greening pattern observed since 2000 by MODIS (FIG. 2c). Recent DGVM studies[122,123] have further confirmed that the carbon sink during the 2000s was partly driven by afforestation and forest regrowth in East Asia and Europe[124]. The extensive greening over croplands, however, has probably contributed less to the carbon sink, because only a minor portion of assimilated carbon by crops remain sequestered due to crop harvest.

The impact of greening on the carbon cycle is also partly responsible for the increasing seasonality of atmospheric CO_2 in the northern high latitudes[125]. The amplitude of the Northern Hemisphere CO_2 seasonal cycle increased by as much as 50% for latitudes north of 45°N[126,127] since the 1960s, indicating enhanced vegetation productivity in northern ecosystems during the carbon-uptake period[128]. The spring zero-crossing date — the time when the detrended seasonal CO_2 variations downcross the zero line in spring — is a phenological indicator of the timing of early season net carbon uptake[125,129]. From 1987 to 2009, the spring zero-crossing date has advanced at high-latitude stations[130] (from −0.5 days decade^{-1} to −1.8 days decade^{-1}) (FIG. 3d), a trend that is consistent with the advancing SOS (FIG. 3b). At the end of the net carbon-uptake period, the autumn zero-crossing dates of detrended seasonal CO_2 variations — the time when the detrended seasonal CO_2 variations up-cross the zero line in autumn — have also advanced over 8 of the 10 Northern Hemisphere stations studied[131]. The observed autumn zero-crossing date advancement (FIG. 3d) is in contrast to the delayed EOS (FIG. 3a) in autumn. This divergence in the autumnal CO_2 and greenness trends suggests that, unlike in spring, autumn vegetation greening does not lead to an increased carbon sink because respiration is increasing faster than photosynthesis in autumn[131]. Visual observations (for example, from the Pan European Phenology Project PEP725) and cameras (for example, PhenoCam datasets) are providing an increasing amount of ground-based phenological evidence of this process. In the future, these data can be paired with eddy covariance flux data, to further our mechanistic understanding of the climate-change-induced seasonal change in greenness and carbon balance.

Biogeophysical impacts of greening

Greening has discernable impacts on the hydrologic cycle and climate through modifying surface biogeophysical properties (for example, albedo, evapotranspiration (ET) and surface roughness) on local to regional and global scales[19,132] (FIG. 7). Vegetation's biogeophysical feedbacks to climate are, thus, critical to understanding the potential of ecosystem management, such as afforestation, for climate change mitigation[3,132,133]. In this section, we present the feedbacks of vegetation greening on the hydrologic cycle and land-surface air temperature.

The hydrologic cycle. Vegetation greening modulates water cycling. Land water losses to the atmosphere occur through ET, which includes transpiration (60–90% of the total land ET[134–136]) and evaporation. Greening increases water losses through an extended area of

Evapotranspiration
(ET). The flux of water emitted from the Earth's surface to the atmosphere. It is the sum of evaporation by the soil, wet canopy, open-water surfaces and transpiration by plant stomata.

Transpiration
The loss of water from plants to the atmosphere.

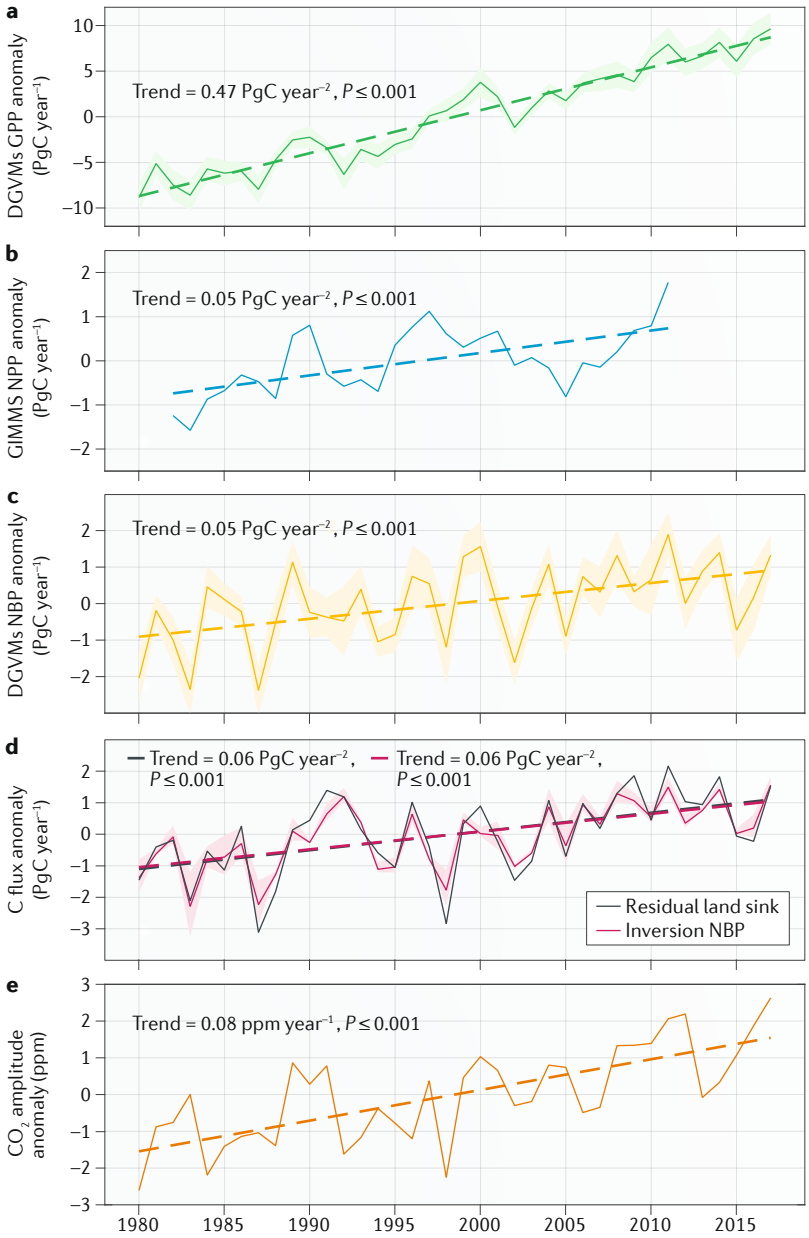

Fig. 6 | **Changes in global carbon fluxes and seasonal CO_2 amplitude.** The graphs depict global gross primary production (GPP) (part **a**), net primary production (NPP) (part **b**), net biome production (NBP) (part **c**), residual land sink (part **d**) and seasonal CO_2 amplitude (part **e**) at Barrow, AK, USA since 1980. The GPP is from the ensemble mean of 16 dynamic global vegetation models (DGVMs)[111]. The NPP is from greenness-based modelling by Smith et al.[198]. The NBP is from the ensemble mean of 16 DGVMs and two atmospheric inversions[111]. Residual land sink is the mass balance residual of anthropogenic CO_2 emissions, the atmospheric CO_2 growth rate and the ocean CO_2 budget[111]. The shaded areas indicate the standard deviation of the GPP, NPP or NBP across models. The dashed lines indicate linear trends.

leaves performing transpiration[137]. A larger foliage area reduces the bare ground surface from which soil evaporation occurs, but increases the re-evaporation of rainfall intercepted by leaves[138], so that greening can cause the net evaporation to either increase or decrease. Various remote-sensing-based ET estimates consistently point to a significant increase in global terrestrial ET over the past four decades, suggesting an intensified water exchange between the land and the atmosphere concurrent with the greening trend[139]. More than half of the global ET increase since the 1980s has been attributed to vegetation greening[138,139] (FIG. 7).

By controlling the changes in ET, vegetation greening also alters the water distribution between regions and water pools (for example, water in soil, rivers and the atmosphere). Assuming that precipitation does not change in response to vegetation greening, a greening-induced ET increase will reduce soil moisture and runoff, which can intensify droughts at the catchment scale[140,141]. In China's Loess Plateau for instance, where intensive afforestation is associated with a pronounced local greening, the river discharge has indeed decreased by a rate of 0.25 km^3 $year^{-2}$ over the past six decades[142]. However, when using ESMs that consider both the greening-induced ET increase and consequent changes in precipitation, simulations forced only with satellite-observed LAI trends do not generate dramatic changes in soil moisture or runoff at continental or global scales[143,144]. This is because greening-induced ET enhancement increases atmospheric water vapour content, which, in turn, promotes downwind precipitation[145,146]. The enhanced precipitation over transpiring regions is particularly evident in moist forests[147] like the Amazon or Congo, which are 'closed' atmospheric systems where 80% of the rainfall originates from upwind ET[145]. Such an efficient atmospheric water recycling mitigates water loss from the soil, sustains inland vegetation and maintains mesic and humid ecosystems.

In addition to intensifying water cycling at the annual scale, vegetation greening also induces seasonal hydrologic changes. There is emerging evidence that spring-greening-enhanced ET leads to a reduction in soil moisture content, which carries over into the following summer and likely suppresses vegetation growth and increases the risk of heatwaves[148,149]. The greening-induced water loss through ET is recycled as land precipitation in subsequent months, benefitting some remote regions through modulating large-scale atmospheric circulation patterns, despite often being insufficient to compensate for evaporative water loss locally[149]. Proposed climate-mitigation strategies, such as afforestation, therefore need to fully consider coupling between vegetation and other components of the Earth system.

Land-surface air temperatures. Greening impacts the exchange of energy between the land and the atmosphere, which ultimately leads to modifications in surface air temperature[150]. Greening increases ET, which cools the surface through evaporative cooling[19,150], but greener canopies have a lower albedo than bare ground and absorb more sunlight, which can result in a larger sensible heat flux. This enhanced sensible heat warms the land surface, an effect called albedo warming[151]. The net effect of greening on surface air temperature in many cases can be viewed as the balance between evaporative cooling and albedo warming[152,153], which was estimated globally to be −0.9 W m^{-2} from evaporative cooling and +0.1 W m^{-2} from albedo warming[19] (FIG. 7c).

Greening can also trigger a series of changes through atmospheric circulation that indirectly affect the surface temperature[154]. For example, the additionally transpired

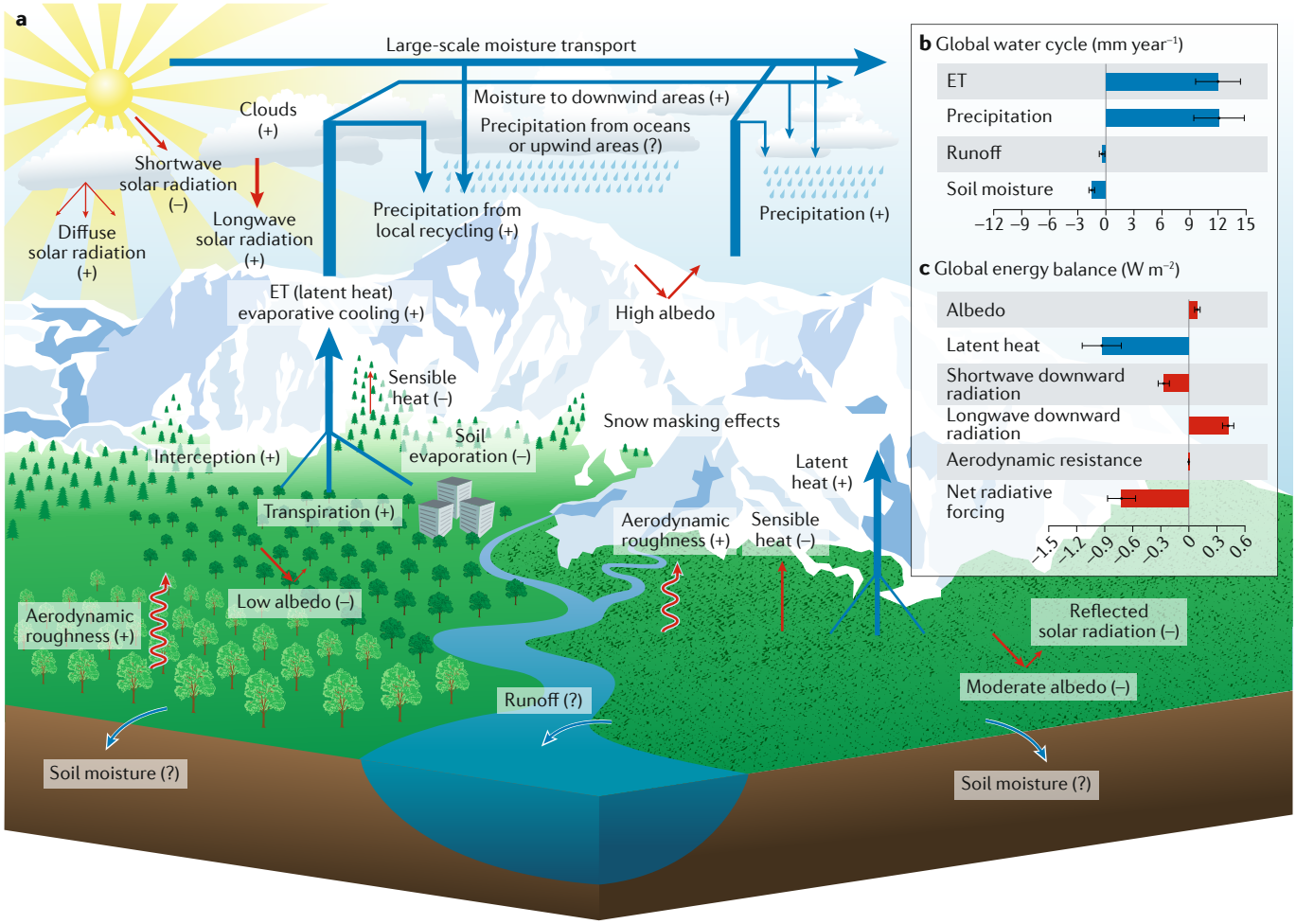

Fig. 7 | **Biogeophysical feedbacks of recent vegetation greening to the climate system. a** | Schematic diagram summarizing land-surface and atmospheric processes through which changes in vegetation greenness feed back into the climate system. For each process or flux, the corresponding symbols '–', '+' and '?' in brackets represent an increasing, decreasing and unknown trend, respectively, in response to vegetation greening, and the colour of arrows represents impacts on water (blue) or energy balance (red, except the latent heat in blue). **b** | Summary of greening-induced changes in major global water cycle fluxes in mm year^{-1} from 1982 to 2011. Data courtesy of Zeng et al.[19]. **c** | Summary of greening-induced changes in global surface energy balance in W m^{-2} from 1982 to 2011. Data courtesy of Zeng et al.[144]. The error bars show the standard error of the estimates. The bar colours are the same as the corresponding fluxes shown in part **a**. ET, evapotranspiration.

water enhances atmospheric water vapour content, which results in more longwave solar radiation entrapment and re-emission in the atmosphere, but reducing the amount of shortwave solar radiation reaching the Earth's surface through increased cloud formation[19,155,156] (FIG. 7). When all the aforementioned impacts of vegetation greening on near-surface air temperature were simulated in coupled ESMs driven by the satellite-based greening since the 1980s, the results suggested a net cooling trend by 12% ± 3% of the concurrent observed warming rate[19].

In warm regions such as the tropics and subtropics, evaporative cooling effects are generally larger than albedo warming effects, leading to a net cooling effect when vegetation greenness increases[19,157,158]. However, the net effect of greening on surface air temperature over the Northern Hemisphere extratropical regions is still subject to debate. Studies based on idealized afforestation and/or deforestation experiments[1,159] or comparisons of the energy budget differences between paired forest and short vegetation sites[132,153] suggested that the albedo warming effect plays a dominant role. These studies, though, assumed complete land cover changes, whereas greening can be gradual. By integrating satellite observations with ESMs, several studies provided an alternative approach that more realistically simulated the effects of vegetation greenness changes and isolated the signal of climate response to greening. These studies found that greening slowed down warming through evaporative cooling in Arctic and boreal regions[19], the Tibetan Plateau[160] and temperate regions like East Asia[161]. Nonetheless, current state-of-the-art modelling efforts are still inconclusive, as some processes are not yet well represented in ESMs, such as snow masking by greener canopies during cold seasons[162–164] and the partitioning of transpiration and evaporation

that is sensitive to vegetation greenness change[136]. Since most ESMs underestimate the ratio of transpiration to ET[136], evaporative cooling by greening could have been underestimated[19,133].

Conclusions

Widespread vegetation greening since the 1980s is one of the most notable characteristics of biosphere change in the Anthropocene. Greening has significantly enhanced the land carbon sink, intensified the hydrologic cycle and cooled the land surface at the global scale. A mechanistic understanding of the underlying drivers shows how anthropogenic forcing has fundamentally altered today's Earth system through a set of feedback loops. Improved knowledge of greenness changes, together with recent progress in observing technology and modelling capacity, has resulted in major advances in understanding global vegetation dynamics. Nonetheless, we still face many challenges ahead.

One key challenge is to continue developing the capacity of remote sensing to measure vegetation structure and functions. Although the vegetation greenness indices described in this Review have proved highly reliable, contemporary satellite greenness products still suffer from limitations, such as inadequate sensitivity to detect changes in dense vegetation, aliasing between snow cover decrease and leaf area increase in cold ecosystems (such as boreal forests), atmospheric contamination, orbital drift and sensor replacements. Compared with the AVHRR, the new moderate-resolution spectral bands and spatial resolutions of 250 m to 1 km of the MODIS sensors on board the Terra (operating since 1999) and Aqua (operating since 2002) satellites have provided global datasets that largely improved the long-term monitoring of vegetation greenness[13]. The current scientific community needs to include Earth observations with higher temporal, richer spectral and finer spatial resolutions to capture various ecosystem functions and processes responding to different parts of the electromagnetic spectrum[165]. We expect the development of next-generation satellite missions and vegetation indices to better fulfil these needs. For example, ongoing efforts on developing hyperspectral remote sensing such as the EnMAP, FLEX, and HyspIRI missions will improve the richness and specificity of spectral information on vegetation structure and functioning.

Another equally important challenge is to validate satellite-based greenness changes with ground observations. Currently, the lack of systematic long-term ground observations covering a large spatial gradient from the high Arctic to the tropics has led to few available ground truths[166] to confirm greenness changes detected through satellite products. Therefore, expanding existing observational networks (such as PhenoCam and FLUXNET) is a high priority. For example, the mismatch between the spatial distribution of vegetation productivity and the density of FLUXNET sites[167] highlights the need to expand the current network from the mid-latitudes to the tropics, where the most photosynthesis takes place. Also, growing crowd-sourced observations by citizen scientists, such as the CrowdCurio phenology observations over the eastern USA[168], can provide valuable data that complement the more expensive professional ground observation networks. These increasing types and amounts of data, together with the rapid development of deep learning[169] and process modelling[11], offer promising tools for improving our understanding of vegetation greening[169].

Considerable uncertainties remain in ESM projections on if and where vegetation greening will occur. Recent studies have identified several processes causing vegetation browning in some regions, including forest diebacks[170], insect[35] and disease outbreaks[171], thermokarst development[172], human mismanagement[36,173], destructive logging[174] and industrial development[175]. These emerging threats could lead to unexpected changes in vegetation greenness relative to our current projections (such as the projections shown in FIGS 2e–h,5), since these processes are under-represented in ESMs. Thus, integrating continued space and ground monitoring and advancing ESM developments is a critical cross-sectoral research priority.

1. Bonan, G. B., Pollard, D. & Thompson, S. L. Effects of boreal forest vegetation on global climate. *Nature* **359**, 716–718 (1992).
2. Haberl, H. et al. Quantifying and mapping the human appropriation of net primary production in earth's terrestrial ecosystems. *Proc. Natl Acad. Sci. USA* **104**, 12942–12947 (2007).
3. Griscom, B. W. et al. Natural climate solutions. *Proc. Natl Acad. Sci. USA* **114**, 11645–11650 (2017).
4. Bastin, J.-F. et al. The global tree restoration potential. *Science* **365**, 76–79 (2019).
5. Tucker, C. J., Fung, I. Y., Keeling, C. D. & Gammon, R. H. Relationship between atmospheric CO_2 variations and a satellite-derived vegetation index. *Nature* **319**, 195–199 (1986).
6. Fung, I. Y., Tucker, C. J. & Prentice, K. C. Application of advanced very high resolution radiometer vegetation index to study atmosphere-biosphere exchange of CO_2. *J. Geophys. Res. Atmos.* **92**, 2999–3015 (1987).
7. Myneni, R. B., Keeling, C. D., Tucker, C. J., Asrar, G. & Nemani, R. R. Increased plant growth in the northern high latitudes from 1981 to 1991. *Nature* **386**, 698–702 (1997).
The first study to reveal large-scale vegetation greening over the Northern Hemisphere.
8. Zhou, L. et al. Variations in northern vegetation activity inferred from satellite data of vegetation index during 1981 to 1999. *J. Geophys. Res. Atmos.* **106**, 20069–20083 (2001).
9. Goetz, S. J., Bunn, A. G., Fiske, G. J. & Houghton, R. A. Satellite-observed photosynthetic trends across boreal North America associated with climate and fire disturbance. *Proc. Natl Acad. Sci. USA* **102**, 13521–13525 (2005).
10. Xu, L. et al. Temperature and vegetation seasonality diminishment over northern lands. *Nat. Clim. Change* **3**, 581–586 (2013).
11. Zhu, Z. et al. Greening of the Earth and its drivers. *Nat. Clim. Change* **6**, 791–795 (2016).
A detailed attribution study of global leaf area index change during the past three decades with ensemble dynamic global vegetation models.
12. Ju, J. & Masek, J. G. The vegetation greenness trend in Canada and US Alaska from 1984–2012 Landsat data. *Remote. Sens. Environ.* **176**, 1–16 (2016).
13. Chen, C. et al. China and India lead in greening of the world through land-use management. *Nat. Sustain.* **2**, 122–129 (2019).
Demonstrated the pattern of global greening since 2000 with the latest MODIS C6 collection data.
14. Lucht, W. et al. Climatic control of the high-latitude vegetation greening trend and Pinatubo effect. *Science.* **296**, 1687–1689 (2002).
15. Arneth, A. et al. IPCC special report on climate change and land. *Intergovernmental Panel on Climate Change (IPCC)* https://www.ipcc.ch/report/srccl/ (2019) (**accessed** October 2019).
16. Abram, N. et al. IPCC special report on the ocean and cryosphere in a changing climate. *Intergovernmental Panel on Climate Change (IPCC)* https://www.ipcc.ch/srocc/home/ (**accessed** October 2019).
17. Eyring, V. et al. Overview of the Coupled Model Intercomparison Project Phase 6 (CMIP6) experimental design and organization. *Geosci. Model. Dev.* **9**, 1937–1958 (2016).
18. Swann, A. L. S., Fung, I. Y. & Chiang, J. C. H. Mid-latitude afforestation shifts general circulation and tropical precipitation. *Proc. Natl Acad. Sci. USA* **109**, 712–716 (2012).
19. Zeng, Z. et al. Climate mitigation from vegetation biophysical feedbacks during the past three decades. *Nat. Clim. Change* **7**, 432–436 (2017).
A quantification of the climatic impacts of vegetation greening through modulating land-atmosphere energy and water exchanges, with an Earth system model forced by satellite-observed leaf area index change during the past three decades.
20. de Jong, R., Verbesselt, J., Schaepman, M. E. & De Bruin, S. Trend changes in global greening and

browning: contribution of short-term trends to longer-term change. *Glob. Change Biol.* **18**, 642–655 (2012).
21. Tian, F. et al. Evaluating temporal consistency of long-term global NDVI datasets for trend analysis. *Remote. Sens. Environ.* **163**, 326–340 (2015).
22. Zhang, Y., Song, C., Band, L. E., Sun, G. & Li, J. Reanalysis of global terrestrial vegetation trends from MODIS products: Browning or greening? *Remote. Sens. Environ.* **191**, 145–155 (2017).
23. Liu, Y., Liu, R. & Chen, J. M. Retrospective retrieval of long-term consistent global leaf area index (1981–2011) from combined AVHRR and MODIS data. *J. Geophys. Res. Biogeosciences* **117**, G04003 (2012).
24. Lyapustin, A. et al. Scientific impact of MODIS C5 calibration degradation and C6+ improvements. *Atmos. Meas. Tech.* **7**, 4353–4365 (2014).
25. Park, T. et al. Changes in growing season duration and productivity of northern vegetation inferred from long-term remote sensing data. *Environ. Res. Lett.* **11**, 084001 (2016).
26. Beck, P. S. A. & Goetz, S. J. Satellite observations of high northern latitude vegetation productivity changes between 1982 and 2008: ecological variability and regional differences. *Environ. Res. Lett.* **6**, 045501 (2011).
27. Sturm, M., Racine, C. & Tape, K. Climate change: increasing shrub abundance in the Arctic. *Nature* **411**, 546–547 (2001).
28. Frost, G. V. & Epstein, H. E. Tall shrub and tree expansion in Siberian tundra ecotones since the 1960s. *Glob. Change Biol.* **20**, 1264–1277 (2014).
29. Myers-Smith, I. H. et al. Climate sensitivity of shrub growth across the tundra biome. *Nat. Clim. Change* **5**, 887–891 (2015).
30. Myers-Smith, I. H. et al. Shrub expansion in tundra ecosystems: dynamics, impacts and research priorities. *Environ. Res. Lett.* **6**, 045509 (2011).
31. Mahowald, N. et al. Projections of leaf area index in earth system models. *Earth Syst. Dyn.* **7**, 211–229 (2016).
32. Bhatt, U. et al. Recent declines in warming and vegetation greening trends over pan-Arctic tundra. *Remote. Sens.* **5**, 4229–4254 (2013).
33. Verbyla, D. The greening and browning of Alaska based on 1982–2003 satellite data. *Glob. Ecol. Biogeogr.* **17**, 547–555 (2008).
34. Senf, C., Pflugmacher, D., Wulder, M. A. & Hostert, P. Characterizing spectral–temporal patterns of defoliator and bark beetle disturbances using Landsat time series. *Remote. Sens. Environ.* **170**, 166–177 (2015).
35. Bjerke, J. W. et al. Understanding the drivers of extensive plant damage in boreal and Arctic ecosystems: Insights from field surveys in the aftermath of damage. *Sci. Total. Environ.* **599**, 1965–1976 (2017).
36. White, J. C., Wulder, M. A., Hermosilla, T., Coops, N. C. & Hobart, G. W. A nationwide annual characterization of 25 years of forest disturbance and recovery for Canada using Landsat time series. *Remote. Sens. Environ.* **194**, 303–321 (2017).
37. Sulla-Menashe, D., Woodcock, C. E. & Friedl, M. A. Canadian boreal forest greening and browning trends: an analysis of biogeographic patterns and the relative roles of disturbance versus climate drivers. *Environ. Res. Lett.* **13**, 014007 (2018).
38. Bi, J., Xu, L., Samanta, A., Zhu, Z. & Myneni, R. Divergent Arctic-boreal vegetation changes between North America and Eurasia over the past 30 years. *Remote. Sens.* **5**, 2093–2112 (2013).
39. Feng, X. et al. Revegetation in China's Loess Plateau is approaching sustainable water resource limits. *Nat. Clim. Change.* **6**, 1019–1022 (2016).
40. Zhou, L. et al. Widespread decline of Congo rainforest greenness in the past decade. *Nature* **509**, 86–90 (2014).
41. Goswami, S., Gamon, J., Vargas, S. & Tweedie, C. Relationships of NDVI, biomass, and leaf area index (LAI) for six key plant species in Barrow, Alaska. *PeerJ PrePrints* **3**, e913v1 (2015).
42. Samanta, A. et al. Amazon forests did not green-up during the 2005 drought. *Geophys. Res. Lett.* **37**, L05401 (2010).
43. Saleska, S. R., Didan, K., Huete, A. R. & Da Rocha, H. R. Amazon forests green-up during 2005 drought. *Science* **318**, 612 (2007).
44. Asner, G. P. & Alencar, A. Drought impacts on the Amazon forest: the remote sensing perspective. *New Phytol.* **187**, 569–578 (2010).
45. Fensholt, R. et al. Greenness in semi-arid areas across the globe 1981–2007—an Earth Observing Satellite based analysis of trends and drivers. *Remote. Sens. Environ.* **121**, 144–158 (2012).
46. Ahlström, A. et al. The dominant role of semi-arid ecosystems in the trend and variability of the land CO_2 sink. *Science* **348**, 895–899 (2015).
47. Buitenwerf, R., Rose, L. & Higgins, S. I. Three decades of multi-dimensional change in global leaf phenology. *Nat. Clim. Change* **5**, 364–368 (2015).
48. Piao, S. et al. Plant phenology and global climate change: current progresses and challenges. *Glob. Change Biol.* **25**, 1922–1940 (2019).
49. White, M. A. et al. Intercomparison, interpretation, and assessment of spring phenology in North America estimated from remote sensing for 1982–2006. *Glob. Change Biol.* **15**, 2335–2359 (2009).
50. Schwartz, M. D. & Hanes, J. M. Intercomparing multiple measures of the onset of spring in eastern North America. *Int. J. Climatol.* **30**, 1614–1626 (2010).
51. Richardson, A. D., Hufkens, K., Milliman, T. & Frolking, S. Intercomparison of phenological transition dates derived from the PhenoCam Dataset V1.0 and MODIS satellite remote sensing. *Sci. Rep.* **8**, 5679 (2018).
52. Jeong, S.-J., Ho, C.-H., Gim, H.-J. & Brown, M. E. Phenology shifts at start vs. end of growing season in temperate vegetation over the Northern Hemisphere for the period 1982–2008. *Glob. Change Biol.* **17**, 2385–2399 (2011).
53. Keenan et al. Net carbon uptake has increased through warming-induced changes in temperate forest phenology. *Nat. Clim. Change* **4**, 598–604 (2014).
54. Garonna, I., de Jong, R. & Schaepman, M. E. Variability and evolution of global land surface phenology over the past three decades (1982–2012). *Glob. Change Biol.* **22**, 1456–1468 (2016).
55. Menzel, A. et al. European phenological response to climate change matches the warming pattern. *Glob. Change Biol.* **12**, 1969–1976 (2006).
56. Cleland, E. E., Chuine, I., Menzel, A., Mooney, H. A. & Schwartz, M. D. Shifting plant phenology in response to global change. *Trends Ecol. Evol.* **22**, 357–365 (2007).
57. Gill, A. L. et al. Changes in autumn senescence in northern hemisphere deciduous trees: a meta-analysis of autumn phenology studies. *Ann. Bot.* **116**, 875–888 (2015).
58. Barichivich, J. et al. Large-scale variations in the vegetation growing season and annual cycle of atmospheric CO_2 at high northern latitudes from 1950 to 2011. *Glob. Change Biol.* **19**, 3167–3183 (2013).
59. Piao, S., Friedlingstein, P., Ciais, P., Viovy, N. & Demarty, J. Growing season extension and its impact on terrestrial carbon cycle in the Northern Hemisphere over the past 2 decades. *Glob. Biogeochem. Cycles* **21**, GB3018 (2007).
60. Julien, Y. & Sobrino, J. A. Global land surface phenology trends from GIMMS database. *Int. J. Remote. Sens.* **30**, 3495–3513 (2009).
61. Park, T. et al. Changes in timing of seasonal peak photosynthetic activity in northern ecosystems. *Glob. Change Biol.* **25**, 2382–2395 (2019).
62. Gonsamo, A., Chen, J. M. & Ooi, Y. W. Peak season plant activity shift towards spring is reflected by increasing carbon uptake by extratropical ecosystems. *Glob. Change Biol.* **24**, 2117–2128 (2018).
63. Bhatt, U. S. et al. Changing seasonality of panarctic tundra vegetation in relationship to climatic variables. *Environ. Res. Lett.* **12**, 055003 (2017).
64. Epstein, H. et al. Tundra greenness. In Arctic Report Card 2018. National Oceanic and Atmospheric Administration (NOAA), 46–52 (2018).
65. Huang, M. et al. Velocity of change in vegetation productivity over northern high latitudes. *Nat. Ecol. Evol.* **1**, 1649–1654 (2017).
66. Farquhar, G. D. & Sharkey, T. D. Stomatal conductance and photosynthesis. *Annu. Rev. Plant. Physiol.* **33**, 317–345 (1982).
67. Keenan, T. F. et al. Increase in forest water-use efficiency as atmospheric carbon dioxide concentrations rise. *Nature* **499**, 324–327 (2013).
68. Donohue, R. J., Roderick, M. L., McVicar, T. R. & Farquhar, G. D. Impact of CO_2 fertilization on maximum foliage cover across the globe's warm, arid environments. *Geophys. Res. Lett.* **40**, 3031–3035 (2013).
69. Ukkola, A. M., Prentice, I. C., Keenan, T. F., van Dijk, A. I. J. M., Viney, N. R., Myneni, R. B. & Bi, J. Reduced streamflow in water-stressed climates consistent with CO_2 effects on vegetation. *Nat. Clim. Change* **6**, 75–78 (2015).
70. Sitch, S. et al. Recent trends and drivers of regional sources and sinks of carbon dioxide. *Biogeosciences* **12**, 653–679 (2015).
71. Ahlbeck, J. R. Comment on "Variations in northern vegetation activity inferred from satellite data of vegetation index during 1981–1999" by L. Zhou et al. *J. Geophys. Res. Atmos.* **107**, ACH–9 (2002).
72. Los, S. O. Analysis of trends in fused AVHRR and MODIS NDVI data for 1982–2006: Indication for a CO_2 fertilization effect in global vegetation. *Glob. Biogeochem. Cycles* **27**, 318–330 (2013).
73. Norby, R. J., Warren, J. M., Iversen, C. M., Medlyn, B. E. & McMurtrie, R. E. CO_2 enhancement of forest productivity constrained by limited nitrogen availability. *Proc. Natl Acad. Sci.USA* **107**, 19368–19373 (2010).
74. Dubey, S. K., Tripathi, S. K. & Pranuthi, G. Effect of elevated CO_2 on wheat crop: Mechanism and impact. *Crit. Rev. Environ. Sci. Technol.* **45**, 2283–2304 (2015).
75. Ainsworth, E. A. & Long, S. P. What have we learned from 15 years of free-air CO_2 enrichment (FACE)? A meta-analytic review of the responses of photosynthesis, canopy properties and plant production to rising CO_2. *New Phytol.* **165**, 351–372 (2005).
76. Norby, R. J. & Zak, D. R. Ecological lessons from free-air CO_2 enrichment (FACE) experiments. *Annu. Rev. Ecol. Evol. Syst.* **42**, 181–203 (2011).
77. Hickler, T. et al. CO_2 fertilization in temperate FACE experiments not representative of boreal and tropical forests. *Glob. Change Biol.* **14**, 1531–1542 (2008).
78. Schimel, D., Stephens, B. B. & Fisher, J. B. Effect of increasing CO_2 on the terrestrial carbon cycle. *Proc. Natl Acad. Sci. USA* **112**, 436–441 (2015).
79. Obermeier, W. A. et al. Reduced CO_2 fertilization effect in temperate C3 grasslands under more extreme weather conditions. *Nat. Clim. Change* **7**, 137–141 (2017).
80. Gray, S. B. et al. Intensifying drought eliminates the expected benefits of elevated carbon dioxide for soybean. *Nat. Plants* **2**, 16132 (2016).
81. Reich, P. B. & Hobbie, S. E. Decade-long soil nitrogen constraint on the CO_2 fertilization of plant biomass. *Nat. Clim. Change* **3**, 278–282 (2013).
82. Reich, P. B., Hobbie, S. E. & Lee, T. D. Plant growth enhancement by elevated CO_2 eliminated by joint water and nitrogen limitation. *Nat. Geosci.* **7**, 920–924 (2014).
83. Terrer, C. et al. Nitrogen and phosphorus constrain the CO_2 fertilization of global plant biomass. *Nat. Clim. Change* **9**, 684–689 (2019).
84. Corlett, R. T. Impacts of warming on tropical lowland rainforests. *Trends Ecol. Evol.* **26**, 606–613 (2011).
85. Huang, M. et al. Air temperature optima of vegetation productivity across global biomes. *Nat. Ecol. Evol.* **3**, 772–779 (2019).
86. Keenan, T. F. & Riley, W. J. Greening of the land surface in the world's cold regions consistent with recent warming. *Nat. Clim. Change* **8**, 825–828 (2018).
87. Braswell, B. H., Schimel, D. S., Linder, E. & Moore, B. III The response of global terrestrial ecosystems to interannual temperature variability. *Science* **278**, 870–873 (1997).
88. Linderholm, H. W. Growing season changes in the last century. *Agric. For. Meteorol.* **137**, 1–14 (2006).
89. Richardson, A. D. et al. Influence of spring and autumn phenological transitions on forest ecosystem productivity. *Philos. Trans. R. Soc. Lond.* **365**, 3227–3246 (2010).
90. Piao, S. et al. Evidence for a weakening relationship between interannual temperature variability and northern vegetation activity. *Nat. Commun.* **5**, 5018 (2014).
Discusses the weakening temperature impacts on northern vegetation greenness since the 1980s.
91. Vickers, H. et al. Changes in greening in the high Arctic: insights from a 30 year AVHRR max NDVI dataset for Svalbard. *Environ. Res. Lett.* **11**, 105004 (2016).
92. Nemani, R. R. et al. Climate-driven increases in global terrestrial net primary production from 1982 to 1999. *Science* **300**, 1560–1563 (2003).
93. Eklundh, L. & Olsson, L. Vegetation index trends for the African Sahel 1982–1999. *Geophys. Res. Lett.* **30**, 1430 (2003).
94. Anyamba, A. & Tucker, C. J. Analysis of Sahelian vegetation dynamics using NOAA-AVHRR NDVI data from 1981–2003. *J. Arid. Environ.* **63**, 596–614 (2005).
95. Donohue, R. J., McVicar, T. R. & Roderick, M. L. Climate-related trends in Australian vegetation cover as inferred from satellite observations, 1981–2006. *Glob. Change Biol.* **15**, 1025–1039 (2009).

96. Herrmann, S. M., Anyamba, A. & Tucker, C. J. Recent trends in vegetation dynamics in the African Sahel and their relationship to climate. *Glob. Environ. Change* **15**, 394–404 (2005).
97. Hickler, T. et al. Precipitation controls Sahel greening trend. *Geophys. Res. Lett.* **32**, L21415 (2005).
98. Huber, S., Fensholt, R. & Rasmussen, K. Water availability as the driver of vegetation dynamics in the African Sahel from 1982 to 2007. *Glob. Planet. Change* **76**, 186–195 (2011).
99. Dardel, C. et al. Re-greening Sahel: 30 years of remote sensing data and field observations (Mali, Niger). *Remote. Sens. Environ.* **140**, 350–364 (2014).
100. Brandt, M. et al. Changes in rainfall distribution promote woody foliage production in the Sahel. *Commun. Biol.* **2**, 133 (2019).
101. Brandt, M. et al. Human population growth offsets climate-driven increase in woody vegetation in sub-Saharan Africa. *Nat. Ecol. Evol.* **1**, 0081 (2017).
102. Curtis, P. G., Slay, C. M., Harris, N. L., Tyukavina, A. & Hansen, M. C. Classifying drivers of global forest loss. *Science* **361**, 1108–1111 (2018).
103. Eighth National Forest Resource Inventory Report (2009–2013) (State Forestry Administration of the People's Republic of China, 2014).
104. Luyssaert, S. et al. Land management and land-cover change have impacts of similar magnitude on surface temperature. *Nat. Clim. Change* **4**, 389–393 (2014).
105. Song, X.-P. et al. Global land change from 1982 to 2016. *Nature* **560**, 639–643 (2018).
106. Poulter, B. et al. The global forest age dataset and its uncertainties (GFADv1.1). *NASA National Aeronautics and Space Administration, PANGAEA* https://doi.org/10.1594/PANGAEA.897392 (2019).
107. Reich, P. B. et al. Nitrogen limitation constrains sustainability of ecosystem response to CO_2. *Nature* **440**, 922–925 (2006).
108. Penuelas, J. et al. Human-induced nitrogen–phosphorus imbalances alter natural and managed ecosystems across the globe. *Nat. Commun.* **4**, 2934 (2013).
109. Greaver, T. L. et al. Key ecological responses to nitrogen are altered by climate change. *Nat. Clim. Change* **6**, 836–843 (2016).
110. Zaehle, S. et al. Evaluation of 11 terrestrial carbon–nitrogen cycle models against observations from two temperate Free-Air CO_2 Enrichment studies. *New Phytol.* **202**, 803–822 (2014).
111. Le Quéré, C. et al. Global carbon budget 2018. *Earth Syst. Sci. Data* **10**, 2141–2194 (2018).
112. Chen, J. M. et al. Vegetation structural change since 1981 significantly enhanced the terrestrial carbon sink. *Nat. Commun.* **10**, 4259 (2019).
113. van Dijk, A. I. J. M., Dolman, A. J. & Schulze, E.-D. Radiation, temperature, and leaf area explain ecosystem carbon fluxes in boreal and temperate European forests. *Glob. Biogeochem. Cycles* **19**, GB2029 (2005).
114. Zhang, Y., Joiner, J., Alemohammad, S. H., Zhou, S. & Gentine, P. A global spatially contiguous solar-induced fluorescence (CSIF) dataset using neural networks. *Biogeosciences* **15**, 5779–5800 (2018).
115. Cheng, L. et al. Recent increases in terrestrial carbon uptake at little cost to the water cycle. *Nat. Commun.* **8**, 110 (2017).
116. Winkler, A. J., Myneni, R. B., Alexandrov, G. A. & Brovkin, V. Earth system models underestimate carbon fixation by plants in the high latitudes. *Nat. Commun.* **10**, 885 (2019).
117. Shevliakova, E. et al. Historical warming reduced due to enhanced land carbon uptake. *Proc. Natl Acad. Sci. USA* **110**, 16730–16735 (2013).
118. Pan, Y. et al. A large and persistent carbon sink in the world's forests. *Science* **333**, 988–993 (2011).
119. Liu, Y. Y. et al. Recent reversal in loss of global terrestrial biomass. *Nat. Clim. Change* **5**, 470–474 (2015).
120. Keenan, T. F. et al. Recent pause in the growth rate of atmospheric CO_2 due to enhanced terrestrial carbon uptake. *Nat. Commun.* **7**, 13428 (2016).
121. Piao, S. et al. Lower land-use emissions responsible for increased net land carbon sink during the slow warming period. *Nat. Geosci.* **11**, 739–743 (2018).
122. Kondo, M. et al. Plant regrowth as a driver of recent enhancement of terrestrial CO_2 uptake. *Geophys. Res. Lett.* **45**, 4820–4830 (2018).
123. Pugh, T. A. M. et al. Role of forest regrowth in global carbon sink dynamics. *Proc. Natl Acad. Sci. USA* **116**, 4382–4387 (2019).
124. Naudts, K. et al. Europe's forest management did not mitigate climate warming. *Science* **351**, 597–600 (2016).
125. Keeling, C. D., Chin, J. F. S. & Whorf, T. P. Increased activity of northern vegetation inferred from atmospheric CO_2 measurements. *Nature* **382**, 146–149 (1996).
126. Graven, H. D. et al. Enhanced seasonal exchange of CO_2 by northern ecosystems since 1960. *Science* **341**, 1085–1089 (2013).
127. Piao, S. et al. On the causes of trends in the seasonal amplitude of atmospheric CO_2. *Glob. Change Biol.* **24**, 608–616 (2018).
128. Forkel, M. et al. Enhanced seasonal CO_2 exchange caused by amplified plant productivity in northern ecosystems. *Science* **351**, 696–699 (2016).
Presents the linkage between increasing photosynthesis of northern vegetation and the enlarging seasonal CO_2 amplitude.
129. Piao, S. et al. Weakening temperature control on the interannual variations of spring carbon uptake across northern lands. *Nat. Clim. Change* **7**, 359–363 (2017).
130. Barichivich, J., Briffa, K. R., Osborn, T. J., Melvin, T. M. & Caesar, J. Thermal growing season and timing of biospheric carbon uptake across the Northern Hemisphere. *Glob. Biogeochem. Cycles* **26**, GB4015 (2012).
131. Piao, S. et al. Net carbon dioxide losses of northern ecosystems in response to autumn warming. *Nature* **451**, 49–52 (2008).
132. Alkama, R. & Cescatti, A. Biophysical climate impacts of recent changes in global forest cover. *Science* **351**, 600–604 (2016).
Presents evidence for feedbacks of forest cover change to land-surface temperature and its regional disparities.
133. Arora, V. K. & Montenegro, A. Small temperature benefits provided by realistic afforestation efforts. *Nat. Geosci.* **4**, 514–518 (2011).
134. Jasechko, S. et al. Terrestrial water fluxes dominated by transpiration. *Nature* **496**, 347–350 (2013).
135. Good, S. P., Noone, D. & Bowen, G. Hydrologic connectivity constrains partitioning of global terrestrial water fluxes. *Science* **349**, 175–177 (2015).
136. Lian, X. et al. Partitioning global land evapotranspiration using CMIP5 models constrained by observations. *Nat. Clim. Change* **8**, 640–646 (2018).
137. Bernacchi, C. J. & VanLoocke, A. Terrestrial ecosystems in a changing environment: a dominant role for water. *Annu. Rev. Plant. Biol.* **66**, 599–622 (2015).
138. Zhang, Y. et al. Multi-decadal trends in global terrestrial evapotranspiration and its components. *Sci. Rep.* **6**, 19124 (2016).
139. Zeng, Z., Peng, L. & Piao, S. Response of terrestrial evapotranspiration to Earth's greening. *Curr. Opin. Environ. Sustain.* **33**, 9–25 (2018).
140. Bosch, J. M. & Hewlett, J. D. A review of catchment experiments to determine the effect of vegetation changes on water yield and evapotranspiration. *J. Hydrol.* **55**, 3–23 (1982).
141. Evaristo, J. & McDonnell, J. J. Global analysis of streamflow response to forest management. *Nature* **570**, 455–461 (2019).
142. Wang, S. et al. Reduced sediment transport in the Yellow River due to anthropogenic changes. *Nat. Geosci.* **9**, 38–41 (2016).
143. Li, Y. et al. Divergent hydrological response to large-scale afforestation and vegetation greening in China. *Sci. Adv.* **4**, eaar4182 (2018).
144. Zeng, Z. et al. Impact of Earth greening on the terrestrial water cycle. *J. Clim.* **31**, 2633–2650 (2018).
145. van der Ent, R. J., Savenije, H. H. G., Schaefli, B. & Steele-Dunne, S. C. Origin and fate of atmospheric moisture over continents. *Water Resour. Res.* **46**, W09525 (2010).
Discusses the importance of land evapotranspiration to sustain downwind precipitation.
146. Teuling, A. J. et al. Observational evidence for cloud cover enhancement over western European forests. *Nat. Commun.* **8**, 14065 (2017).
147. Spracklen, D. V., Arnold, S. R. & Taylor, C. M. Observations of increased tropical rainfall preceded by air passage over forests. *Nature* **489**, 282–285 (2012).
148. Buermann, W. et al. Widespread seasonal compensation effects of spring warming on northern plant productivity. *Nature* **562**, 110–114 (2018).
149. Lian, X. et al. Summer soil drying exacerbated by earlier spring greening of northern vegetation. *Sci. Adv.* (in the press).
150. Bonan, G. B. Forests, climate, and public policy: A 500-year interdisciplinary odyssey. *Annu. Rev. Ecol. Evol. Syst.* **47**, 97–121 (2016).
151. Davin, E. L. & de Noblet-Ducoudré, N. Climatic impact of global-scale deforestation: Radiative versus nonradiative processes. *J. Clim.* **23**, 97–112 (2010).
152. Bonan, G. B. Forests and climate change: forcings, feedbacks, and the climate benefits of forests. *Science* **320**, 1444–1449 (2008).
153. Lee, X. et al. Observed increase in local cooling effect of deforestation at higher latitudes. *Nature* **479**, 384–387 (2011).
154. Winckler, J., Lejeune, Q., Reick, C. H. & Pongratz, J. Nonlocal effects dominate the global mean surface temperature response to the biogeophysical effects of deforestation. *Geophys. Res. Lett.* **46**, 745–755 (2019).
155. Green, J. K. et al. Regionally strong feedbacks between the atmosphere and terrestrial biosphere. *Nat. Geosci.* **10**, 410–414 (2017).
156. Devaraju, N., de Noblet-Ducoudré, N., Quesada, B. & Bala, G. Quantifying the relative importance of direct and indirect biophysical effects of deforestation on surface temperature and teleconnections. *J. Clim.* **31**, 3811–3829 (2018).
157. Bateni, S. M. & Entekhabi, D. Relative efficiency of land surface energy balance components. *Water Resour. Res.* **48**, 4510 (2012).
158. Forzieri, G., Alkama, R., Miralles, D. G. & Cescatti, A. Satellites reveal contrasting responses of regional climate to the widespread greening of Earth. *Science* **356**, 1180–1184 (2017).
159. Betts, R. A. Offset of the potential carbon sink from boreal forestation by decreases in surface albedo. *Nature* **408**, 187–190 (2000).
160. Shen, M. et al. Evaporative cooling over the Tibetan Plateau induced by vegetation growth. *Proc. Natl Acad. Sci. USA* **112**, 9299–9304 (2015).
161. Jeong, S., Ho, C., Kim, K. & Jeong, J. Reduction of spring warming over East Asia associated with vegetation feedback. *Geophys. Res. Lett.* **36**, L18705 (2009).
162. Essery, R. Large-scale simulations of snow albedo masking by forests. *Geophys. Res. Lett.* **40**, 5521–5525 (2013).
163. Thackeray, C. W., Fletcher, C. G. & Derksen, C. The influence of canopy snow parameterizations on snow albedo feedback in boreal forest regions. *J. Geophys. Res. Atmos.* **119**, 9810–9821 (2014).
164. Wang, L. et al. Investigating the spread in surface albedo for snow-covered forests in CMIP5 models. *J. Geophys. Res. Atmos.* **121**, 1104–1119 (2016).
165. National Academies of Sciences, Engineering, and Medicine. Thriving on our changing planet: A decadal strategy for Earth observation from space (National Academies Press, 2018) https://doi.org/10.17226/24938.
166. Metcalfe, D. B. et al. Patchy field sampling biases understanding of climate change impacts across the Arctic. *Nat. Ecol. Evol.* **2**, 1443–1448 (2018).
167. Schimel, D. et al. Observing terrestrial ecosystems and the carbon cycle from space. *Glob. Change Biol.* **21**, 1762–1776 (2015).
168. Park, D. S. et al. Herbarium specimens reveal substantial and unexpected variation in phenological sensitivity across the eastern United States. *Philos. Trans. R. Soc. Lond. B Biol. Sci.* **374**, 20170394 (2018).
169. Reichstein, M. et al. Deep learning and process understanding for data-driven Earth system science. *Nature* **566**, 195–204 (2019).
170. Allen, C. D. et al. A global overview of drought and heat-induced tree mortality reveals emerging climate change risks for forests. *For. Ecol. Manage.* **259**, 660–684 (2010).
171. Sturrock, R. N. et al. Climate change and forest diseases. *Plant. Pathol.* **60**, 133–149 (2011).
172. Raynolds, M. K. & Walker, D. A. Increased wetness confounds Landsat-derived NDVI trends in the central Alaska North Slope region, 1985–2011. *Environ. Res. Lett.* **11**, 085004 (2016).
173. Matasci, G. et al. Three decades of forest structural dynamics over Canada's forested ecosystems using Landsat time-series and lidar plots. *Remote. Sens. Environ.* **216**, 697–714 (2018).
174. Mitchard, E. T. A. The tropical forest carbon cycle and climate change. *Nature* **559**, 527–534 (2018).

175. Esau, I., Miles, V. V., Davy, R., Miles, M. W. & Kurchatova, A. Trends in normalized difference vegetation index (NDVI) associated with urban development in northern West Siberia. *Atmos. Chem. Phys.* **16**, 9563–9577 (2016).
176. Knyazikhin, Y. et al. Hyperspectral remote sensing of foliar nitrogen content. *Proc. Natl Acad. Sci. USA* **110**, E185–E192 (2013).
177. Tucker, C. J. Red and photographic infrared linear combinations for monitoring vegetation. *Remote. Sens. Environ.* **8**, 127–150 (1979).
178. Bannari, A., Morin, D., Bonn, F. & Huete, A. R. A review of vegetation indices. *Remote. Sens. Rev.* **13**, 95–120 (1995).
179. Myneni, R. B., Hall, F. G., Sellers, P. J. & Marshak, A. L. The interpretation of spectral vegetation indexes. *IEEE Trans. Geosci. Remote. Sens.* **33**, 481–486 (1995).
180. Xue, J. & Su, B. Significant remote sensing vegetation indices: A review of developments and applications. *J. Sens.* **2017**, 1353691 (2017).
181. Ganguly, S. et al. Generating vegetation leaf area index Earth system data record from multiple sensors. Part 2: Implementation, analysis and validation. *Remote. Sens. Environ.* **112**, 4318–4332 (2008).
182. Zhu, Z. et al. Global data sets of vegetation leaf area index (LAI) 3g and fraction of photosynthetically active radiation (FPAR) 3g derived from global inventory modeling and mapping studies (GIMMS) normalized difference vegetation index (NDVI3g) for the period 1981 to 2011. *Remote. Sens.* **5**, 927–948 (2013).
183. Pinzon, J. & Tucker, C. A non-stationary 1981–2012 AVHRR NDVI3g time series. *Remote. Sens.* **6**, 6929–6960 (2014).
Discusses some complexities and challenges in detecting greenness change with the longest available NDVI dataset (AVHRR NDVI) since the 1980s.
184. Knyazikhin, Y., Martonchik, J. V., Myneni, R. B., Diner, D. J. & Running, S. W. Synergistic algorithm for estimating vegetation canopy leaf area index and fraction of absorbed photosynthetically active radiation from MODIS and MISR data. *J. Geophys. Res. Atmos.* **103**, 32257–32275 (1998).
185. Chen, J. M. & Black, T. A. Defining leaf area index for non-flat leaves. *Plant. Cell Environ.* **15**, 421–429 (1992).
186. Asrar, G. Q., Fuchs, M., Kanemasu, E. T. & Hatfield, J. L. Estimating absorbed photosynthetic radiation and leaf area index from spectral reflectance in wheat 1. *Agron. J.* **76**, 300–306 (1984).
187. Cohen, W. B., Maiersperger, T. K., Gower, S. T. & Turner, D. P. An improved strategy for regression of biophysical variables and Landsat ETM+ data. *Remote. Sens. Environ.* **84**, 561–571 (2003).
188. Baret, F. et al. GEOV1: LAI and FAPAR essential climate variables and FCOVER global time series capitalizing over existing products. Part1: Principles of development and production. *Remote. Sens. Environ.* **137**, 299–309 (2013).
189. Claverie, M., Matthews, J., Vermote, E. & Justice, C. A 30+ year AVHRR LAI and FAPAR climate data record: Algorithm description and validation. *Remote. Sens.* **8**, 263 (2016).
190. Ross, J. K. & Marshak, A. L. Calculation of canopy bidirectional reflectance using the Monte Carlo method. *Remote. Sens. Environ.* **24**, 213–225 (1988).
191. Yang, B. et al. Estimation of leaf area index and its sunlit portion from DSCOVR EPIC data: Theoretical basis. *Remote. Sens. Environ.* **198**, 69–84 (2017).
192. Xiao, Z. et al. Long-time-series global land surface satellite leaf area index product derived from MODIS and AVHRR surface reflectance. *IEEE Trans. Geosci. Remote. Sens.* **54**, 5301–5318 (2016).
193. Myneni, R., Knyazikhin, Y. & Park, T. MOD15A2H MODIS/terra leaf area index/FPAR 8-day L4 global 500 m SIN grid V006. *NASA EOSDIS L. Process. DAAC* (2015).
194. Tucker, C. J. et al. An extended AVHRR 8-km NDVI dataset compatible with MODIS and SPOT vegetation NDVI data. *Int. J. Remote. Sens.* **26**, 4485–4498 (2005).
195. Huete, A. et al. Overview of the radiometric and biophysical performance of the MODIS vegetation indices. *Remote. Sens. Environ.* **83**, 195–213 (2002).
196. Maisongrande, P., Duchemin, B. & Dedieu, G. VEGETATION/SPOT: an operational mission for the Earth monitoring; presentation of new standard products. *Int. J. Remote. Sens.* **25**, 9–14 (2004).
197. Badgley, G., Field, C. B. & Berry, J. A. Canopy near-infrared reflectance and terrestrial photosynthesis. *Sci. Adv.* **3**, e1602244 (2017).
198. Smith, W. K. et al. Large divergence of satellite and Earth system model estimates of global terrestrial CO_2 fertilization. *Nat. Clim. Change* **6**, 306–310 (2016).

Acknowledgements
This study was supported by the National Natural Science Foundation of China (41861134036) and the Research Council of Norway (grant no. 287402), the National Key R&D Program of China (2017YFA0604702) and the Thousand Youth Talents Plan project in China. The works of C.C., R.B.M. and T.P. were funded by NASA's Earth Science Division. The authors thank Z. Zhu, Y. Li, K. Wang, Y. Deng, M. Gao and X. Li for their help in preparing the manuscript.

Author contributions
S.P., X.W., T.P., C.C., X.L., Y.H., J.W.B., A.C., P.C., H.T. and R.B.M. wrote the first draft of the manuscript. S.P., X.W. and R.B.M. reviewed and edited the manuscript before submission. All authors made substantial contributions to the discussion of content.

Competing interests
The authors declare no competing interests.

Publisher's note
Springer Nature remains neutral with regard to jurisdictional claims in published maps and institutional affiliations.

Reviewer information
Nature Reviews Earth & Environment thanks the three anonymous reviewers, for their contribution to the peer review of this work.

Supplementary information
Supplementary information is available for this paper at https://doi.org/10.1038/s43017-019-0001-x.

RELATED LINKS
PEP725: http://www.pep725.eu
PhenoCam: http://www.phenocam.us
EnMAP: http://www.enmap.org/
FLEX: https://Earth.esa.int/web/guest/missions/esa-future-missions/flex
HyspIRI: https://hyspiri.jpl.nasa.gov/
FLUXNET: https://fluxnet.fluxdata.org/

QUERY FORM

Nature Reviews Earth & Environment	
Manuscript ID	**1**
Author	**Shilong Piao**

AUTHOR:

The following queries have arisen during the editing of your manuscript. Please answer by making the requisite corrections directly in the e.proofing tool rather than marking them up on the PDF. This will ensure that your corrections are incorporated accurately and that your paper is published as quickly as possible.

Query No.	*Nature of Query*
Q1:	in the original manuscript, reference 38 appeared before references 32–38, so this has been adjusted also.
Q2:	Please check your article carefully, coordinate with any co-authors and enter all final edits clearly in the eproof, remembering to save frequently. Once corrections are submitted, we cannot routinely make further changes to the article.
Q3:	Note that the eproof should be amended in only one browser window at any one time; otherwise changes will be overwritten.
Q4:	Author surnames have been highlighted. Please check these carefully and adjust if the first name or surname is marked up incorrectly. Note that changes here will affect indexing of your article in public repositories such as PubMed. Also, carefully check the spelling and numbering of all author names and affiliations, and the corresponding email address(es).
Q5:	You cannot alter accepted Supplementary Information files except for critical changes to scientific content. If you do resupply any files, please also provide a brief (but complete) list of changes. If these are not considered scientific changes, any altered Supplementary files will not be used, only the originally accepted version will be published.

Supplement information for:

Characteristics, drivers and feedbacks of global greening

Shilong Piao[1,2,3*], Xuhui Wang[1], Taejin Park[4], Chi Chen[4], Xu Lian[1], Yue He[1], Jarle W. Bjerke[5], Anping Chen[6], Philippe Ciais[1,7], Hans Tømmervik[5], Ramakrishna R. Nemani[8], Ranga B. Myneni[4]

[1] Sino-French Institute for Earth System Science, College of Urban and Environmental Sciences, Peking University, Beijing 100871, China.

[2] Key Laboratory of Alpine Ecology and Biodiversity, Institute of Tibetan Plateau Research, Chinese Academy of Sciences, Beijing 100085, China.

[3] Center for Excellence in Tibetan Earth Science, Chinese Academy of Sciences, Beijing 100085, China.

[4] Department of Earth and Environment, Boston University, Boston, MA 02215, USA.

[5] Norwegian Institute for Nature Research, FRAM – High North Research Centre for Climate and the Environment, PO Box 6606, Tromsø NO-9296, Norway.

[6] Department of Biology, Colorado State University, Fort Collins, CO 80523, USA.

[7] Laboratoire des Sciences du Climat et de l'Environnement, CEA CNRS UVSQ, Gif-sur-Yvette 91191, France.

[8] NASA Ames Research Center, Moffett Field, CA 94035, USA.

* Correspondence should be addressed to Shilong Piao (slpiao@pku.edu.cn)

Table. S1 | Categorization of vegetation indices based on three derivative forms of surface reflectance with respect to wavelength. Details for the derivative forms can be found in ref. 1.

Type	Vegetation Index
Type 1	NDVI (Normalized Difference Vegetation Index; ref. 2), SR (Simple Ration; ref. 3), SAVI (Soil Adjusted Vegetation Index; ref. 4), TSAVI (Transformed Soil Adjusted Vegetation Index; ref. 5), OSAVI (Optimized Soil Adjusted Vegetation Index; ref. 6), PVI (Perpendicular Vegetation Index; ref. 7), WDVI (Weighted Difference Vegetation Index; ref. 8), GCI (Green Chlorophyll Index, ref. 9), GNDVI (Green Normalized Difference Vegetation Index; ref. 10), GRVI (Green Ratio Vegetation Index; ref. 11), PRI (Photochemical Reflectance Index; ref. 12), DVI (Difference Vegetation Index; ref. 13), NDWI (Normalized Difference Water Index; ref. 14), CCI (Chlorophyll/Carotenoid Index; ref. 15)
Type 2	GEMI (Global Environmental Monitoring Index; ref. 16), Greenness (ref. 17), NLI (Non-Linear Index; ref.18), NIRv (Near-Infrared Reflectance of Vegetation, ref. 19)
Type 3	EVI (Enhanced Vegetation Index, ref. 20), ARVI (Atmospherically Resistant Vegetation Index; ref. 21), SARVI (Soil Adjusted and Atmospherically Resistant Vegetation Index; ref. 21), GARI (Green Atmospherically Resistant Index; ref. 22)

Table. S2 | Summary of satellite global NDVI products.

NDVI Product	Time span	Data input source	Ground Sampling Distance	Frequency	Reference
MODIS[#,*]	2000 (2002) – Present	Terra(Aqua)/MODIS C6 reflectance	250 m, 500 m, 1 km, and 0.05º	16-day & Monthly	Ref. 23
VIIRS[#,*]	2012 - Present	Suomi-NPP/VIIRS reflectance	500 m, 1 km, and 0.05º	16-day & Monthly	Ref. 24
DSCOVR[#]	2015 – Present	DSCOVR/EPIC reflectance	10 km	Hourly & daily	Ref. 25
NDVI3g	1981 - 2018	AVHRR GAC level-1b data	1/12º	Biweekly	Ref. 26
VIP4	1981 - 2016	LTDR3 AVHR09C1 and MOD09CMG data	0.05º	Daily, 7-day, 15-day, monthly	Ref. 27
LTDR5[#]	1981 - Present	AVHRR GAC level-1b data	0.05º	Daily	Ref. 28
CGLS[#] (or GEOV2)	1999 - Present	SPOT/VGT & PROVA-V reflectance	1/112º	10-day	Ref. 29

[#]: The product has been operationally generated, archived, and disseminated.

[*]: EVI (Enhanced Vegetation Index) is also available in this product.

Table. S3 | Comparison of data and processing from AVHRR, MODIS, SPOT-VGT and MERIS sensors.

AVHRR	MODIS	SPOT-VGT	MERIS
Broad red and near-infrared wavelength channels. These are not necessarily chosen to be responsive to changes in vegetation as these are meteorological sensors.	Narrow red and near-infrared wavelength channels designed specifically to respond to vegetation changes [30].	Moderately narrow red and near-infrared wavelength channels designed specifically to respond to vegetation changes[31].	Very narrow red and near-infrared wavelength channels designed specifically to respond to vegetation changes.
No on-board calibration. Sensor calibrated before launch, but loses calibration over time[32].	On-board calibration. Sensor calibrated before launch and during operation regularly. The sensor is also periodically calibrated using the moon[33].	No on-board calibration. Sensor calibrated before launch, but loses calibration over time[31].	Sensor calibrated before launch and during operation regularly. MERIS on-board calibration is based on on-board measurements of sunlight[34].
Multiple sequential sensors with little or no overlap[26]. Each sensor data span is about 3 to 4 years. Inter-sensor data calibration is a major problem.	Two near-simultaneous sensors. The Terra MODIS data stream started in Feb 2000 (Aqua MODIS stream started in May 2002). Overlaps allows inter-sensor calibration.	Two sensors. VEGETATION 1 (VGT1) on board SPOT4, launched in March 1998, and VEGETATION 2 (VGT2) on board SPOT5 launched in May 2002[35]. After February 2003, VGT1 has no longer been used for VI products. Overlaps allows inter-sensor calibration.	One sensor. The ENVISAT MERIS LAI data stream started in July 2002 and ended in March 2012[36]. No official products for NDVI and EVI.

Satellite loses orbit over time. Data is collected over progressively lower and lower sun angles[37]. Variations in data due to sun angle changes are conflated with changes in vegetation.	Both Terra and Aqua platforms maintain precise orbits. Any orbit loss is periodically corrected by pushing the satellites into their designated orbits. Variations in data due to changes in sun-sensor geometry are explicitly considered during LAI retrievals[38,39] .	The signal is stable. Irradiance variations due to sun-earth distance and sun-sensor geometry are explicitly corrected[31].	Orbital information is unknown.
Minimal correction for atmospheric contamination of signals emanating from vegetation. Sensor lacks additional wavelength channels required for accurate cloud screening, correction for daily tropospheric aerosol contamination and periodic stratospheric aerosol contamination (following volcanic eruptions)[40].	Sensor has several channels that are used to accurately screen for clouds, including high cirrus. Atmospheric correction for molecular and tropospheric aerosol contamination is performed accurately with a radiative transfer-based algorithm on a daily basis for each of the seven vegetation channels[41,42].	A simplified physics-based atmospheric correction algorithm (based on the 6S method) is employed for water vapor, ozone, and tropospheric aerosol[31].	Several different radiative transfer-based algorithms are used for atmospheric correction for aerosol optical thickness, columnar water vapor and surface reflectance, as well as for LAI retrieval[36,43].
As no physics-based processing is possible with AVHRR channel data. NDVI and EVI generally corresponds to the data with minimal	The physics-based processing removes atmospheric effects and provides users with at-ground reflectance data for each of the seven	A simplified physics-based processing removes atmospheric effects and provides users with at-ground reflectance data for NDVI	No official products available for NDVI and EVI. Various approaches were proposed based on top of atmosphere reflectance and surface

atmospheric contamination[26,44].	channels, and for NDVI and EVI products[20,42].	and EVI products.	reflectance.
LAI products are derived using black-box approaches such as neural nets. Partial validation with ground measurements[40]. No suitable field data prior to 2000 exist for validation.	The channel reflectance data are used in other physics-based algorithms to derive leaf area estimates[39,45] . The derived products are extensively validated with ground measurements[46]. All the algorithms have been periodically updated and the entire archive is re-processed to produce newer versions of the data products.	LAI products are derived using black-box approaches i.e., neural networks. The product has been extensively validated with ground measurements[47].	The LAI retrieval based on the BEAM MERIS vegetation processor. This algorithm is trained by neural networks with a suite of simulated top-of-atmosphere radiances, using the Scattering by Arbitrarily Inclined Leaves (SAIL), PROSPECT and a simplified method for atmospheric correction[36].
Low spatial resolution (8×8 km^2) and 15-day frequency for the period July 1981 to December 2016[26,40].	Moderate spatial resolution (500×500 m^2), 8-day/16-day frequency for the period Feb 2000 to Dec 2018[20,46,48].	1/112° ×1/112° spatial resolution (1×1 km^2), 10-day frequency for the period 1999-present[47].	1/360° ×1/360° spatial resolution (300×300 m^2), 10-day frequency for the from 2002-2012[36].

33 **Table. S4 | Summary of satellite global LAI products.**

LAI Product	Time span	Data input source	Ground Sampling Distance	Frequency	Algorithm	Reference
MODIS[#]	2000 (2002) – Present	Terra(Aqua)/MODIS C6 reflectance	500 m	8-day (4-day for Terra/Aqua combined)	LUT based on 3D RT	Ref. 46,48
VIIRS[#]	2012 – Present	Suomi-NPP/VIIRS reflectance	500 m	8-day	LUT based on 3D RT	Ref. 49
DSCOVR[#]	2015 – Present	DSCOVR/EPIC reflectance	10 km	Hourly & daily	LUT based on 3D RT	Ref. 50
LAI3g	1981 – 2018	GIMMS NDVI3g	1/12º	Biweekly	ANN trained with MODIS LAI	Ref. 40
GLASS	1981 – 2017	NOAA/AVHRR LTDR reflectance & Terra/MODIS C6 reflectance	0.05º (1km available from 2000)	8-day	GRNN trained with CYCLOPES and MODIS LAIs	Ref. 51
TCDR[#]	1981 – Present	NOAA/AVHRR TCDR reflectance	0.05º	Daily	ANN trained with MODIS LAI	Ref. 52
GLOBMAP	1981 – 2017	GIMMS NDVI & Terra/MODIS C6 reflectance	1/13.75º	Biweekly, 1982 – 1999/2 8-day, 2000/3 – 2017	LUT based on RT	Ref. 53

CGLS[#] (or GEOV2)	1999 – Present	SPOT/VGT & PROVA-V reflectance	1/112º	10-day	ANN trained with CYCLOPES and MODIS LAIs	Ref. 29
MERIS	2002-2012	ENVISAT/MERIS reflectance	1/360º	10-day	ANN trained with 1D RT	Ref. 36

[#]: The product has been operationally generated, archived, and disseminated.

Data Archives

MODIS: https://earthdata.nasa.gov/
VIIRS: https://earthdata.nasa.gov/
GLASS: http://globalchange.bnu.edu.cn/research/lai
TCDR: https://www.ncei.noaa.gov/data/avhrr-land-leaf-area-index-and-fapar/access/
LAI3g: http://sites.bu.edu/cliveg/datacodes/
GLOBMAP: http://www.globalmapping.org/
CGLS LAI: https://land.copernicus.eu/global/products/lai
CGLS NDVI: https://land.copernicus.eu/global/products/ndvi
NDVI3g: https://ecocast.arc.nasa.gov/data/pub/gimms/3g.v1/
VIP4: https://vip.arizona.edu/viplab_data_explorer.php
LTDR5: https://ltdr.modaps.eosdis.nasa.gov/cgi-bin/ltdr/ltdrPage.cgi?fileName=products

Table. S5 | CMIP5 models used in this study.

Model abbreviation	historical	RCP2.6	RCP4.5	RCP6.0	RCP8.5
bcc-csm1-1	√	√	√	√	√
Bcc-csm1-1-m	√	√	√	√	√
BNU-ESM	√	√	√		√
CCSM4	√	√	√	√	
CESM1-BGC	√		√		√
CESM1-CAM5	√	√	√	√	√
CanESM2	√	√	√		√
GFDL-CM3	√		√		
GFDL-ESM2G	√	√		√	√
GFDL-ESM2M	√		√	√	√
HadGEM2-CC	√		√		√
HadGEM2-ES	√	√	√	√	√
IPSL-CM5A-LR	√	√	√	√	√
IPSL-CM5A-MR	√	√	√	√	√
MIROC-ESM-CHEM	√	√	√	√	√
MIROC-ESM	√	√	√	√	√
MPI-ESM-LR	√	√	√		√
MPI-ESM-MR	√	√	√		√
NorESM1-ME	√	√	√	√	√
NorESM1-M	√	√	√	√	√
inmcm4	√		√		√

References

1. Myneni, R. B. *et al.* The meaning of spectral vegetation indices. *IEEE Trans. Geosc. Remote Sens.* **33**, 481-486 (1995).
2. Rouse, J., Haas, R.H., Schell, J.A. & Deering, D.W. Monitoring vegetation systems in the Great Plains with ERTS. *In Proceedings of the 3rd ERTS Symposium, Washington DC, USA, NASA SP-351*, 309-317 (1974).
3. Birth, G. S., & McVey, G. R. Measuring the color of growing turf with a reflectance spectrophotometer 1. *Agron. J.* **60**, 640-643 (1968).
4. Huete, A.R. A soil-adjusted vegetation index (SAVI). *Remote Sens. Environ.* **25**, 295-309 (1988).
5. Baret, F., Guyot, G. and Major, D.J. TSAVI: a vegetation index which minimizes soil brightness effects on LAI and APAR estimation. *In 12th Canadian Symposium on Remote Sensing Geoscience and Remote Sensing Symposium* **3**, 1355-1358 (1989).
6. Rondeaux, G., Steven, M. & Baret, F. Optimization of soil-adjusted vegetation indices. *Remote Sens. Environ.* **55**, 95-107. (1996).
7. Richardson, A.J. & Wiegand, C.L. Distinguishing vegetation from soil background information. *Photogramm. Eng. Remote Sens.* **43**, 1541-1552 (1977).
8. Clevers, J.G.P.W. Application of a weighted infrared-red vegetation index for estimating leaf area index by correcting for soil moisture. *Remote Sens. Environ.* **29**, 25-37 (1989).
9. Gitelson, A.A., Gritz, Y. & Merzlyak, M.N. Relationships between leaf chlorophyll content and spectral reflectance and algorithms for non-destructive chlorophyll

74 assessment in higher plant leaves. *J. Plant Physiol.* **160**, 271-282 (2003).
75 10. Gitelson, A.A. & Merzlyak, M.N. Remote sensing of chlorophyll concentration in higher
76 plant leaves. *Adv. Space Res.* **22**, 689-692 (1998).
77 11. Sripada, R.P., Heiniger, R.W., White, J.G. & Meijer, A.D. Aerial color infrared
78 photography for determining early in-season nitrogen requirements in corn. *Agron. J.* **98**,
79 968-977 (2006).
80 12. Gamon, J.A., Penuelas, J. & Field, C.B. A narrow-waveband spectral index that tracks
81 diurnal changes in photosynthetic efficiency. *Remote Sens. Environ.* **41**, 35-44 (1992).
82 13. Tucker, C.J. Red and photographic infrared linear combinations for monitoring vegetation.
83 *Remote Sens. Environ.* **8**, 127-150 (1979).
84 14. McFeeters, S.K. The use of the Normalized Difference Water Index (NDWI) in the
85 delineation of open water features. *Int. J. Remote Sens.* **17**, 1425-1432 (1996).
86 15. Gamon, J.A. *et al*. A remotely sensed pigment index reveals photosynthetic phenology in
87 evergreen conifers. *Proc. Natl. Acad. Sci. U.S.A.* **113**, 13087-13092 (2016).
88 16. Pinty, B. & Verstraete, M.M. GEMI: a non-linear index to monitor global vegetation from
89 satellites. *Vegetatio* **101**, 15-20 (1992).
90 17. Jackson, R.D. Spectral indices in n-space. *Remote Sens. Environ.* **13**, 409-421 (1983).
91 18. Goel, N.S. & Qin, W. Influences of canopy architecture on relationships between various
92 vegetation indices and LAI and FPAR: A computer simulation. *Remote Sens. Rev.* **10**,
93 309-347 (1994).
94 19. Badgley, G., Field, C. B. & Berry, J. A. Canopy near-infrared reflectance and terrestrial

photosynthesis. *Sci. Adv.* **3**, e1602244 (2017).

20. Huete, A., Didan, K., Miura, T., Rodriguez, E. P., & Gao, X. Overview of the radiometric and biophysical performance of the MODIS vegetation indices. *Remote Sens. Environ.* **83**, 195-213 (2002).

21. Kaufman, Y.J. & Tanre, D. Atmospherically resistant vegetation index (ARVI) for EOS-MODIS. *IEEE Trans. Geosci. Remote Sens.* **30**, 261-270 (1992).

22. Gitelson, A.A., Kaufman, Y.J. & Merzlyak, M.N. Use of a green channel in remote sensing of global vegetation from EOS-MODIS. *Remote Sens. Environ.* **58**, 289-298 (1996).

23. Didan, K., Munoz, A.B., Solano, R. & Huete, A., MODIS vegetation index user's guide (MOD13 series). *Vegetation Index and Phenology Lab, The University of Arizona,* 1-38 (2015).

24. Didan, K., Munoz, A.B., Compton, J.T. & Pinzon, J.E. Suomi-VIIRS Vegetation Index Product Suite User Guide & Abridged Algorithm Theoretical Basis Document. *Vegetation Index and Phenology Lab, The University of Arizona,* 1-100 (2017).

25. Knyazikhin, Y., Song, W., Yang, B., Park, T. & Myneni, R.B. DSCOVR EPIC Vegetation Earth System Data Record Science Data Product Guide (2018).

26. Pinzon, E. J. & Tucker, J. C. A Non-Stationary 1981–2012 AVHRR NDVI3g Time Series. *Remote Sens.* **6**, 6929-6960 (2014).

27. Barreto-munoz, A., Didan, K., Miura, T. & Tsend-Ayush, J. December. Version 4 of the Vegetation Index and Phenology Earth Science Data Records. *In AGU Fall Meeting*

Abstracts (2014).

28. Pedelty, J. *et al*. Generating a long-term land data record from the AVHRR and MODIS instruments. *In 2007 IEEE International Geoscience and Remote Sensing Symposium* 1021-1025 (2007).
29. Baret, F., *et al.* GEOV1: LAI and FAPAR essential climate variables and FCOVER global time series capitalizing over existing products. Part1: Principles of development and production. *Remote Sens. Environ.* **137**, 299-309 (2013).
30. Justice, C. O., Townshend, J., & Vermote, E. F. An overview of MODIS Land data processing and product status. *Remote Sens. Environ.* **83**, 3-15 (2002).
31. Toté, C. *et al.* Evaluation of the SPOT/VEGETATION Collection 3 reprocessed dataset_ Surface reflectances and NDVI. *Remote Sens. Environ.* **201**, 219-233 (2017).
32. Staylor, W. F. Degradation rates of the AVHRR visible channel for the NOAA 6, 7, and 9 spacecraft. *J. Atmos. Oceanic Technol.* **7**, 411-423 (1990).
33. Xiong, X., Wu, A., & Cao, C. On-orbit calibration and inter-comparison of Terra and Aqua MODIS surface temperature spectral bands. *Int. J. Remote Sens.* **29**, 5347-5359 (2008).
34. Bourg, L., & Delwart, S. MERIS instrument calibration. *In Second MERIS and AATSR Calibration and Geophysical Validation Workshop, Frascati, Italy* 20-24 (2006).
35. Deronde, B. *et al.* 15 years of processing and dissemination of SPOT-VEGETATION products. *Int. J. Remote Sens.* **35**, 2402-2420 (2014).
36. Tum, M., *et al*. Global gap-free MERIS LAI time series (2002–2012). *Remote Sens.* **8**, 69

(2016).

37. Kaufman, R. K. *et al.* Effect of orbital drift and sensor changes on the time series of AVHRR vegetation index data. *IEEE Trans. Geosci. Remote Sens.* **38**, 2584-2597 (2000).

38. Knyazikhin, Y. *et al.* Synergistic algorithm for estimating vegetation canopy leaf area index and fraction of absorbed photosynthetically active radiation from MODIS and MISR data. *J. Geophys. Res. D: Atmos.* **103**, 32257-32275 (1998).

39. Myneni, R. B. *et al*. Increased plant growth in the northern high latitudes from 1981 to 1991. *Nature* **386**, 698-702 (1997).

40. Zhu, Z. *et al.* Global Data Sets of Vegetation Leaf Area Index (LAI)3g and Fraction of Photosynthetically Active Radiation (FPAR)3g Derived from Global Inventory Modeling and Mapping Studies (GIMMS) Normalized Difference Vegetation Index (NDVI3g) for the Period 1981 to 2011. *Remote Sens.* **5**, 927-948 (2013).

41. Frey, R. A. *et al.* Cloud Detection with MODIS. Part I: Improvements in the MODIS Cloud Mask for Collection 5. *J. Atmos. Oceanic Technol.* **25**, 1057-1072 (2008).

42. Vermote, E. F., Saleous, El, N. Z., & Justice, C. O. Atmospheric correction of MODIS data in the visible to middle infrared: first results. *Remote Sens. Environ.* **83**, 97-111 (2002).

43. Guanter, L., Gómez-Chova, L., & Moreno, J. Coupled retrieval of aerosol optical thickness, columnar water vapor and surface reflectance maps from ENVISAT/MERIS data over land. *Remote Sens. Environ.***112**, 2898-2913 (2008).

44. Holben, B. N. Characteristics of maximum-value composite images from temporal

AVHRR data. *Int. J. Remote Sens.* **7**, 1417-1434 (1986).

45. Knyazikhin, Y. *et al.* Estimation of vegetation canopy leaf area index and fraction of absorbed photosynthetically active radiation from atmosphere-corrected MISR data. *J. Geophys. Res. D: Atmos.* **103**, 32239-32256 (1998).

46. Yan, K. *et al.* Evaluation of MODIS LAI/FPAR Product Collection 6. Part 2: Validation and Intercomparison. *Remote Sens.* **8**, 460 (2016).

47. Verger, A., Baret, F., & Weiss, M. GEOV2/VGT: near real time estimation of global biophysical variables from VEGETATION-P data. *In MultiTemp 2013: 7th International Workshop on the Analysis of Multi-Temporal Remote Sensing Images*, 1-4 (2013).

48. Yan, K. *et al.* Evaluation of MODIS LAI/FPAR Product Collection 6. Part 1: Consistency and Improvements. *Remote Sens.* **8**, 359 (2016).

49. Yan, K. *et al.* Generating global products of lai and fpar from snpp-viirs data: Theoretical background and implementation. *IEEE Trans. Geosci. Remote Sens.* **56**, 2119-2137 (2018).

50. Yang, B., *et al.* Estimation of leaf area index and its sunlit portion from DSCOVR EPIC data: Theoretical basis. *Remote Sens. Environ.* **198**, 69-84 (2017).

51. Xiao, Z., Liang, S., Wang, T., & Jiang, B. Retrieval of Leaf Area Index (LAI) and Fraction of Absorbed Photosynthetically Active Radiation (FAPAR) from VIIRS Time-Series Data. *Remote Sens.* **8**, 351 (2016).

52. Claverie, M., Matthews, J., Vermote, E. & Justice, C. A 30+ year AVHRR LAI and FAPAR climate data record: Algorithm description and validation. *Remote Sens.* **8**, 263

(2016).

53. Liu, Y., Liu, R., & Chen, J. M. Retrospective retrieval of long-term consistent global leaf area index (1981-2011) from combined AVHRR and MODIS data. *J. Geophys. Res. Biogeosci.* **117**, G04003 (2012).